Cell

Resource

Two-photon synthetic aperture microscopy for minimally invasive fast 3D imaging of native subcellular behaviors in deep tissue

Graphical abstract

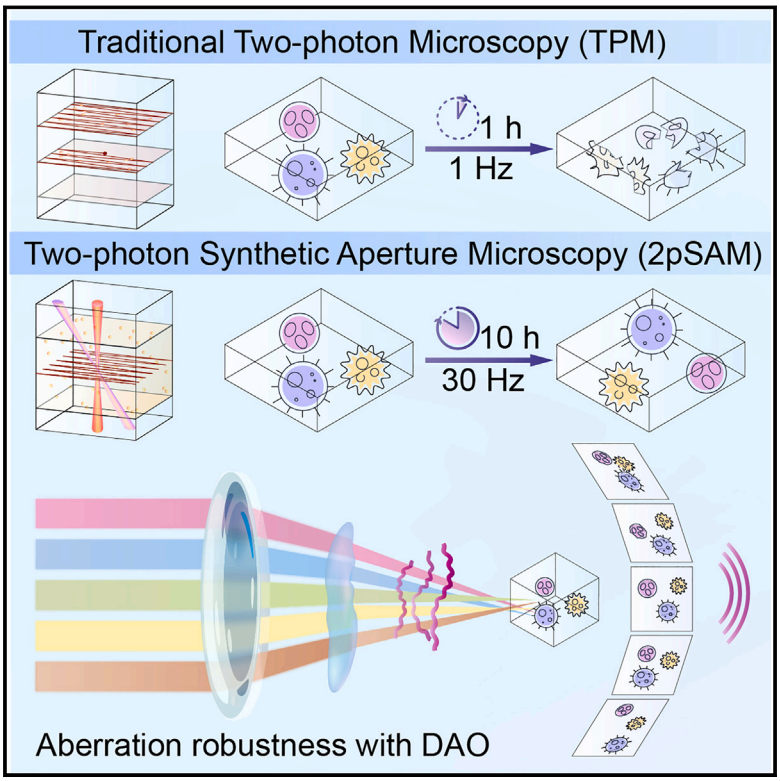

Highlights

- 2pSAM enables long-term fast subcellular 3D imaging in deep tissue by needle beams
- Phototoxicity of traditional two-photon imaging is reduced by orders of magnitude
- Multisite aberration correction is achieved at high speed with a compact system
- 2pSAM visualized complete germinal-center formation during immune response

Authors

Zhifeng Zhao, Yiliang Zhou, Bo Liu, ..., Jiamin Wu, Hai Qi, Qionghai Dai

Correspondence

wujiamin@tsinghua.edu.cn (J.W.), qihai@tsinghua.edu.cn (H.Q.), daiqh@tsinghua.edu.cn (Q.D.)

In brief

Harnessing the concept of synthetic aperture radar in two-photon microscopy, 2pSAM offers aberration-corrected 3D imaging of subcellular dynamics at a millisecond scale over large volumes in deep tissue, with reduced phototoxicity to enable challenging continuous long-term *in vivo* imaging applications in mice.

Zhao et al., 2023, Cell *186*, 1–17
May 25, 2023
https://doi.org/10.1016/j.cell.2023.04.016

CellPress

Cell

CellPress
OPEN ACCESS

Resource

Two-photon synthetic aperture microscopy for minimally invasive fast 3D imaging of native subcellular behaviors in deep tissue

Zhifeng Zhao,[1,2,3,4,5,13] Yiliang Zhou,[1,2,3,4,5,13] Bo Liu,[6,7,8,13] Jing He,[1,2,3,4,13] Jiayin Zhao,[1,2,3,9] Yeyi Cai,[1,2,3,4] Jingtao Fan,[1,2,3] Xinyang Li,[1,2,3,5,9] Zilin Wang,[2,10] Zhi Lu,[1,2,3,4,5] Jiamin Wu,[1,2,3,4,*] Hai Qi,[6,7,8,11,12,*] and Qionghai Dai[1,2,3,4,14,*]

[1]Department of Automation, Tsinghua University, Beijing 100084, China
[2]Institute for Brain and Cognitive Sciences, Tsinghua University, Beijing 100084, China
[3]Beijing Key Laboratory of Multi-dimension & Multi-scale Computational Photography (MMCP), Tsinghua University, Beijing 100084, China
[4]IDG/McGovern Institute for Brain Research, Tsinghua University, Beijing 100084, China
[5]Hangzhou Zhuoxi Institute of Brain and Intelligence, Hangzhou 311100, China
[6]Tsinghua-Peking Center for Life Sciences, Beijing 100084, China
[7]Laboratory of Dynamic Immunobiology, Institute for Immunology, Tsinghua University, Beijing 100084, China
[8]Department of Basic Medical Sciences, School of Medicine, Tsinghua University, Beijing 100084, China
[9]Tsinghua Shenzhen International Graduate School, Tsinghua University, Shenzhen 518071, China
[10]Department of Anesthesiology, the First Medical Center, Chinese PLA General Hospital, Beijing 100853, China
[11]Beijing Key Laboratory for Immunological Research on Chronic Diseases, Tsinghua University, Beijing 100084, China
[12]Beijing Frontier Research Center for Biological Structure, Tsinghua University, Beijing 100084, China
[13]These authors contributed equally
[14]Lead contact
*Correspondence: wujiamin@tsinghua.edu.cn (J.W.), qihai@tsinghua.edu.cn (H.Q.), daiqh@tsinghua.edu.cn (Q.D.)
https://doi.org/10.1016/j.cell.2023.04.016

SUMMARY

Holistic understanding of physio-pathological processes requires noninvasive 3D imaging in deep tissue across multiple spatial and temporal scales to link diverse transient subcellular behaviors with long-term physiogenesis. Despite broad applications of two-photon microscopy (TPM), there remains an inevitable tradeoff among spatiotemporal resolution, imaging volumes, and durations due to the point-scanning scheme, accumulated phototoxicity, and optical aberrations. Here, we harnessed the concept of synthetic aperture radar in TPM to achieve aberration-corrected 3D imaging of subcellular dynamics at a millisecond scale for over 100,000 large volumes in deep tissue, with three orders of magnitude reduction in photobleaching. With its advantages, we identified direct intercellular communications through migrasome generation following traumatic brain injury, visualized the formation process of germinal center in the mouse lymph node, and characterized heterogeneous cellular states in the mouse visual cortex, opening up a horizon for intravital imaging to understand the organizations and functions of biological systems at a holistic level.

INTRODUCTION

Long-term observation of cellular and subcellular behaviors and functions in deep tissue can provide invaluable insights for pathology,[1] immunology,[2] neuroscience,[3,4] cell biology,[5] and developmental biology.[6] Owing to the long wavelength and nonlinear property for deep penetration, two-photon microscopy (TPM) has facilitated enormous discoveries in the past decades with the development of various animal models.[7–9] However, the point-scanning scheme, accumulated phototoxicity, and optical aberrations result in inevitable tradeoff among spatiotemporal resolution, imaging volume, and imaging durations,[10–13] restricting panoramic understanding of complicated biological phenomena across multiple spatial and temporal scales. For example, it is difficult to track cellular migrations or neural firing across the entire process of immune responses[14] or memory formation.[15] Instrumental developments linking these transient cellular or subcellular dynamics with long-term physio-pathogenesis may help to understand fundamental organizations and functional mechanisms of biological systems at the holistic level.[16,17]

Although various high-speed three-dimensional (3D) two-photon microscopes have been developed, these approaches either require high laser power to generate multiple foci[18–22] or spatiotemporal sparse priors for specific applications such as localization or neural recoding.[23–27] Bessel-focus scanning

Please cite this article in press as: Zhao et al., Two-photon synthetic aperture microscopy for minimally invasive fast 3D imaging of native subcellular behaviors in deep tissue, Cell (2023), https://doi.org/10.1016/j.cell.2023.04.016

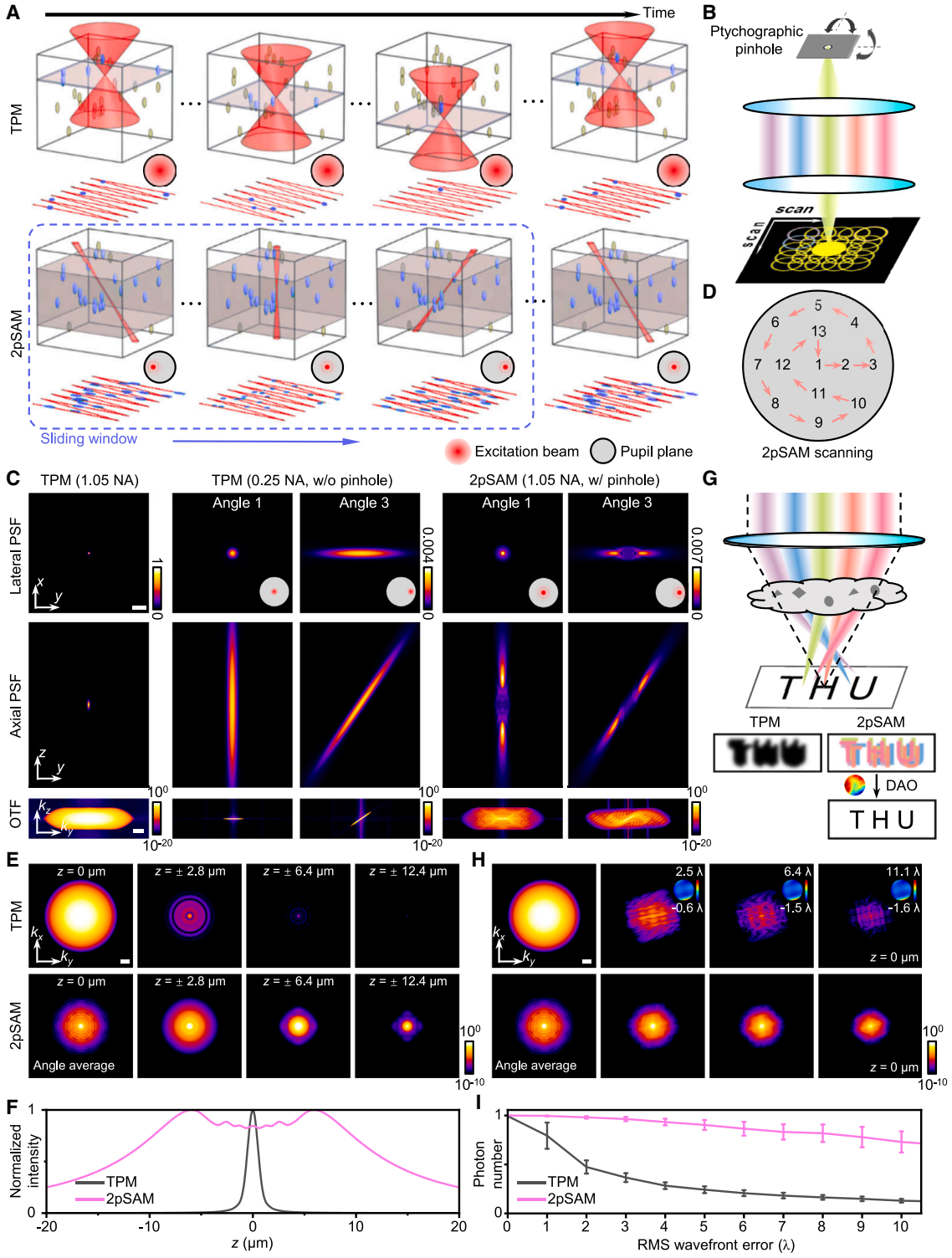

Figure 1. Principle of 2pSAM

(A) Concept comparison between TPM and 2pSAM.

(B) The ptychographic pinhole at the focal point of the needle beam for aperture synthesis.

(C) Comparisons of PSFs and 3D OTFs among TPM (1.05 NA full-aperture excitation), TPM (0.25-NA sub-aperture excitation without the pinhole), and mid-NA 2pSAM (0.105-NA sub-aperture excitation with the pinhole).

(D) The scanning order and corresponding distributions of the sub-aperture at the back-pupil plane.

(legend continued on next page)

Please cite this article in press as: Zhao et al., Two-photon synthetic aperture microscopy for minimally invasive fast 3D imaging of native subcellular behaviors in deep tissue, Cell (2023), https://doi.org/10.1016/j.cell.2023.04.016

TPM samples a large volume rapidly by extending the depth of field (DOF) while sacrificing axial resolution.[28,29] Moreover, TPM are sensitive to optical aberrations due to the nonlinear response. Although adaptive optics (AO) can address the problem with improved resolution and signal-to-noise-ratio (SNR), it requires an additional wavefront sensor or a spatial light modulator to estimate and compensate wavefront distortions in scattering tissue or imperfect imaging systems,[11,30] which normally have a small effective field of view (FOV) due to spatially nonuniform aberrations.[31,32] Therefore, long-term high-speed high-resolution 3D imaging in deep tissue remains an unsolved systemic challenge.

To address these problems while minimizing phototoxicity, we present a two-photon synthetic aperture microscopy (2pSAM) by capturing multiple angular projections of the entire 3D volume with needle-like beams instead of point scanning with a high numerical aperture (NA). We find that accumulated nonlinear photodamage is underestimated in traditional TPM during long-term continuous imaging even with the laser power far below the previously characterized safety threshold. 2pSAM can not only achieve subcellular 3D imaging at the millisecond scale in deep tissue with significant reduction in phototoxicity (corresponding to over 1,000-fold slower photobleaching rate than TPM) but also show strong robustness against various kinds of optical aberrations. With its capabilities, we identified direct intercellular communications through migrasomes following traumatic brain injury (TBI), visualized the complete formation process of a germinal center (GC) during an immune response, and revealed heterogeneous cellular states during hour-long high-speed large-scale neural recording in mice.

RESULTS

Principle of 2pSAM

The concept of synthetic aperture origins from the radar, representing the conversion from angular resolution to 3D spatial resolution.[33] We harnessed this concept in two-photon imaging to better collect photons in 3D. As shown in Figure 1A, by excitation at different sub-apertures of the back-pupil plane, we can obtain different angular projections of 3D volumes with an extended DOF, which can be synthesized to retrieve axial information through 3D deconvolution, akin to computed tomography (Video S1, part I). Compared with traditional point-excitation TPM, needle excitation with extended DOF provides a more efficient way for 3D imaging by making full use of the light power during propagation, sharing the same spirit of light-sheet microscopy[34] and light-field microscopy.[35] In this case, we can obtain similar emission photons with lower peak power density at the elongated foci for orders of magnitude reduction in nonlinear photodamage.[36–38]

However, excitation with a low-NA sub-aperture results in low resolution, making it impractical to observe subcellular behaviors *in vivo*. It is hard to synthesize sub-aperture images directly for high resolution like radar, since emission fluorescence is incoherent and we can only detect the intensity without phase information. To address this problem, we exploit the concept of electron ptychography[39] by adding a pinhole with a size close to the Abbe diffraction limit of low-NA excitation at the focal point, which introduces the same spatial constraint for different angular beams, facilitating the synthesis of sub-apertures close to the diffraction limit of whole-objective NA (Figures 1B and S1A). The sharp edge of the pinhole reshapes point spread functions (PSFs) of different angles and extends the frequency coverage throughout the entire pupil due to diffraction, preserving high-frequency information (Figure 1C). Different from 3D spatial scanning used in high-NA TPM, 2pSAM scans needle-like beams across two-dimensional (2D) spatial domains and 2D angular domains (Figure 1D). Therefore, 3D voxels are not sampled separately in the spatial domain with a uniform 3D optical transfer function (OTF) but are multiplexed in different combinations akin to the tomographic process encoded by multiple angular PSFs with emphasis on different spatial frequencies. A 3D phase-space deconvolution algorithm[5] is used to reconstruct high-resolution volumes iteratively (Figures S1B–S1E; STAR Methods).

A large pinhole size reduces synthesized resolution due to the attenuation of diffraction effects, whereas a narrow pinhole size can increase high-frequency responses at the cost of DOF and laser power (Figures S2A–S2D). Smaller excitation NA increases the volume coverage but requires more angles to reconstruct high-resolution volumes, especially for dense structures (Figures S2A–S2H). Since reconstruction performance converges with about 13 angles for most cases in simulation (Figures S2G–S2I), we set the angle number as 13 with a uniform distribution in the back-pupil plane. Then, by adjusting the ratio α between sub-aperture NA and whole-objective NA, we can balance the effective DOF and spatial resolution with a fixed angle number. For most experiments, we choose $\alpha = 0.1$ for slightly reduced resolution but with a depth coverage of about 25 μm.

With the same excitation power, we find the total fluorescence intensities in 3D collected by 2pSAM and TPM are similar to an ideal imaging system and environment. The elongated PSF excites a much larger volume due to the extended DOF, albeit with a smaller peak power during nonlinear excitation than a tight high-NA focus, as indicated by 2D OTFs and energy distributions at different axial planes (Figures 1E and 1F). Such a schematic

(E) 2D OTFs of TPM and 2pSAM (mid) at different axial planes using logarithmic scales. We use the average 2D OTF of 13 angles for 2pSAM. The OTFs are normalized by the maximum of all layers.
(F) Normalized axial energy distribution of PSFs for TPM and 2pSAM (mid).
(G) DAO in 2pSAM.
(H) 2D OTFs of TPM and 2pSAM (mid) with different levels of aberration, normalized by the maximum of the non-aberrated OTF.
(I) Curves of total photon number excited by PSF in 3D versus increasing aberrations introduced for TPM and 2pSAM (mid, angle 1). We normalize curves by the total photon number of TPM without aberration. Aberrations are indicated by the root mean square (RMS) of the wavefront errors. We used mean ± standard deviation here (n = 100 randomly generated aberrations). All OTFs are displayed on a logarithmic scale.
Scale bars: 5 μm and 1 μm^{-1} in (C) and 1 μm^{-1} in (E) and (H). See also Figures S1–S3.

Please cite this article in press as: Zhao et al., Two-photon synthetic aperture microscopy for minimally invasive fast 3D imaging of native subcellular behaviors in deep tissue, Cell (2023), https://doi.org/10.1016/j.cell.2023.04.016

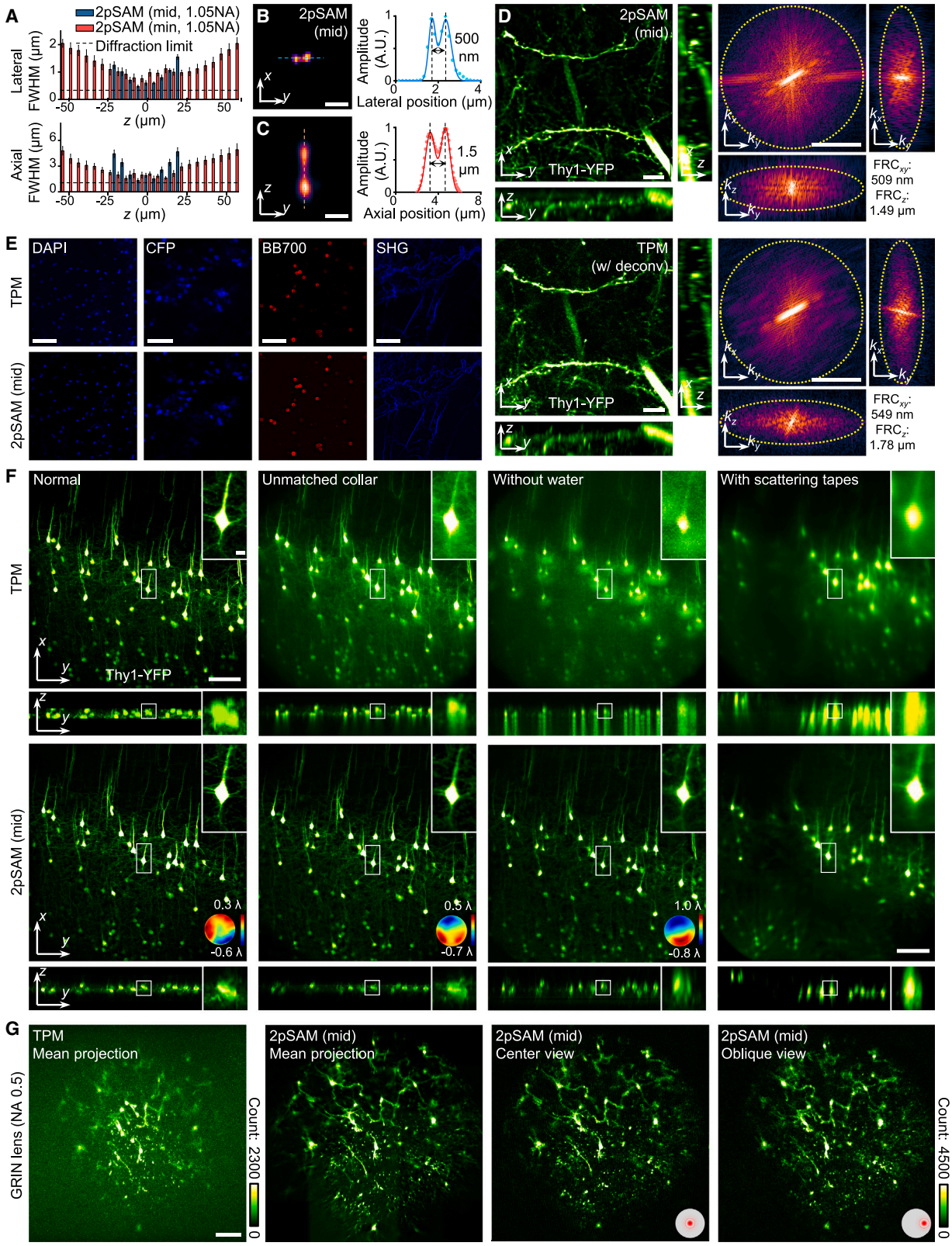

(legend on next page)

greatly reduces nonlinear photodamages while maintaining a similar SNR. More importantly, nonuniform distributions of the refractive index in tissue or imperfect imaging systems will distort excitation wavefronts regarded as optical aberrations resulting in reduced resolution and SNRs (Figure 1G). 2pSAM captures sub-aperture components separately rather than mixing them up coherently, leading to much better aberration robustness than TPM (Figure 1H). Although the total excited fluorescence intensity of high-NA TPM decreases quickly with an increase of aberrations, raw measurements of 2pSAM sustain consistent SNRs in 3D (Figure 1I). With a pinhole as the spatial constraint, the equivalent aberration at the pupil plane leads to lateral shifts of different angular PSFs, corresponding to phase gradients of different sub-apertures (Figure S2J). Aberrated wavefront can then be inferred without additional wavefront sensors[40] (Figure S2K). We then perform aberration correction digitally during 3D deconvolution by replacing ideal PSFs with aberrated PSFs to retrieve native 3D fluorescence distributions. By dividing the FOV into multiple tiles during reconstruction, we can achieve multisite aberration correction without reducing the imaging speed. We call the entire process digital AO (DAO), which has recently been verified in one-photon imaging and photography,[5,41] but never explored in TPM due to the lack of high-resolution aberration-robust angular measurements.

In addition, as 13 angles are required to reconstruct a volume in 2pSAM, the net rate of 3D imaging for 2pSAM is about 2.3 volume/s with the sampling of 512 × 512 × 13 ($x \times y \times$ angle) pixels for each volume. However, for time-lapse continuous data, as we scan angles periodically with each measurement containing the projection of entire volume, we can increase temporal resolution with a sliding window during 3D deconvolution (Figures 1A and S3A), which has already been widely applied in spiral computed tomography and magnetic resonance imaging.[42] By exploiting spatiotemporal continuity and estimating motions during reconstruction,[43,44] we developed a motion-correction algorithm to avoid motion artifacts during scanning and increase reconstruction volumetric speed to 30 volume/s. We conducted numerical simulations for the quantitative evaluation of morphological movements and functional intensity changes. Even for motions up to 96 μm/s under the 25×/1.05NA objective, 3D resolution can be well preserved without artifacts at 30 Hz (Figures S3B–S3D). Although only 1 iteration is required for high-contrast samples, more iterations can increase motion robustness for 3D samples with smooth structures (Figure S3E). Transient temporal responses such as calcium activities obtained with the sliding window show a significantly higher correlation to ground truth (GT) data than those without the sliding window (Figures S3F–S3H).

Experimental characterizations of 2pSAM

To verify the framework, we built up a system that could flexibly switch among three configurations including traditional TPM, mid-NA 2pSAM (α = 0.1, to achieve a subcellular resolution with an effective volumetric range of 25 μm), and min-NA 2pSAM (α = 0.05, to achieve an effective volumetric range of 100 μm with a slightly reduced resolution) (Figure S1A; Table S1). We first characterized resolutions by imaging 200 nm diameter fluorescence beads, corresponding to the full width at a half-maximum (FWHM) of 508 ± 43 nm (mid-NA) and 759 ± 97 nm (min-NA) laterally, 1,315 ± 136 nm (mid-NA) and 1,573 ± 156 nm (min-NA) axially (mean ± standard deviation, n = 413 beads; Figure 2A). The resolution gradually decreases with an increase of defocus distances, resulting in the effective axial range larger than 25 μm for mid-NA 2pSAM (average lateral resolution <1 μm, average axial resolution <2 μm) and 100 μm for min-NA 2pSAM (average lateral resolution <2 μm, average axial resolution <4 μm). We further verified the resolution of mid-NA 2pSAM by resolving virtually separated two points, generated by adding images of the same bead captured with a 500-nm lateral interval or a 1.5-μm axial interval (Figures 2B and 2C). Moreover, we imaged the Thy1-YFP mouse brain tissue to resolve synapse structures (with a lateral resolution of 509 ± 11 nm and axial resolution of 1,490 ± 61 nm estimated by Fourier ring correlation (FRC),[45] n = 10 slices; Figure 2D), compared with the traditional TPM. With an optical parametric oscillator system in the laser, we can tune excitation wavelengths across a broad range for diverse samples such as 4',6-diamidino-2-phenylindole (DAPI), cyan fluorescent protein (CFP), BB700, and collagen structures with second-harmonic generation. As the framework is independent of wavelengths, 2pSAM has a similar performance across different wavelengths compared with TPM (Figure 2E).

To further demonstrate the aberration robustness of 2pSAM with DAO, we imaged the same Thy1-YFP mice brain tissue under the same laser power with 4 kinds of aberrations including normal condition, unmatched collar correction, loss of water

Figure 2. Resolution characterization of 2pSAM

(A) Boxplots of lateral and axial resolutions for mid-NA 2pSAM and min-NA 2pSAM at different axial positions. The resolution is estimated by FWHMs of intensity profiles with a Gaussian fit for 200-nm-diameter beads distributed in 1% agarose (n = 400 beads, >10 beads per plane). We used mean ± standard deviation here. Diffraction limits are indicated by dashed lines.

(B) MIP of two virtually spaced beads in *xy* plane with a 500-nm lateral interval by mid-NA 2pSAM.

(C) MIP of two virtually spaced beads in *yz* plane with a 1,500-nm axial interval by mid-NA 2pSAM.

(D) Orthogonal MIPs of Thy1-YFP brain slice imaged by mid-NA 2pSAM and TPM. Fourier ring correlation (FRC) was used to estimate lateral and axial resolutions. Dashed yellow rings indicate the diffraction limits.

(E) Comparisons between TPM and 2pSAM (mid) on different wavelength for samples labeled by DAPI, CFP, and BB700 and second harmonic generation (SHG).

(F) Comparisons between TPM and 2pSAM (mid) on the same sample with the same power in the conditions of different aberrations (from left to right: normal, unmatched objective collar, water loss under the water-immersion objective, and imaging through the scattering tapes).

(G) Comparisons between TPM and 2pSAM (mid) on endoscopic imaging for the same area through the 0.5-NA GRIN lens implanted in the cortex of a CX3CR1-GFP mouse under the same power (Video S1, part I). Both raw measurements and reconstructed mean intensity projections are compared. The reconstructed projection is generated from multiple small tiles stitched together for multi-site aberration correction.

Scale bar: 1 μm (B and C), 10 μm, 1 μm^{-1} (D), 50 μm (E), 100 μm, 10 μm (for zoom-in views) (F), and 100 μm (G).

Please cite this article in press as: Zhao et al., Two-photon synthetic aperture microscopy for minimally invasive fast 3D imaging of native subcellular behaviors in deep tissue, Cell (2023), https://doi.org/10.1016/j.cell.2023.04.016

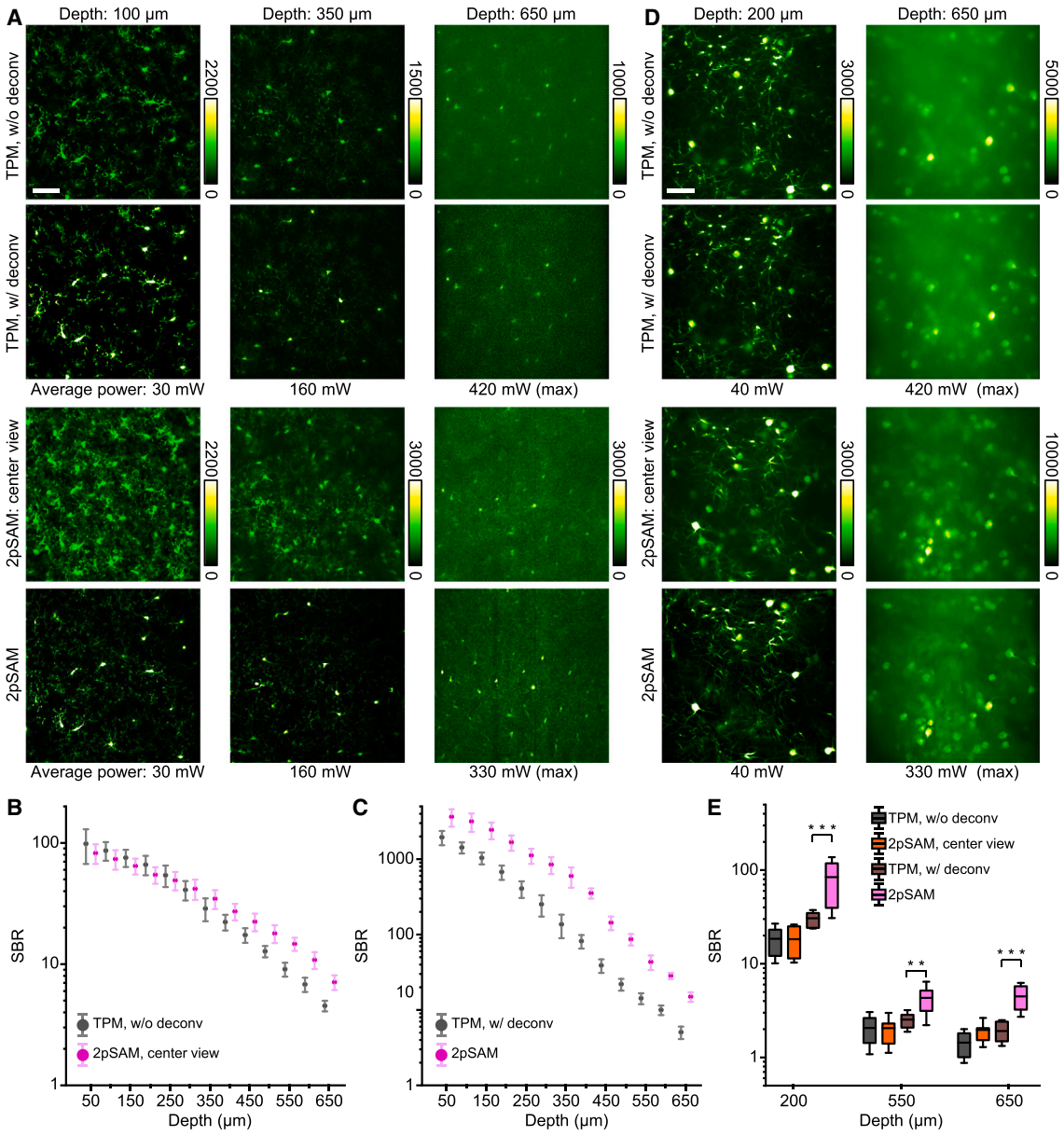

Figure 3. 2pSAM facilitates deep penetration comparable with TPM

(A) Imaging results of the cortex in the same CX3CR1-GFP mouse obtained at different depths by TPM and 2pSAM (mid). We compared the slice obtained by TPM with and without deconvolution, raw center view of mid-NA 2pSAM, and the reconstructed slice. Excitation powers are marked at the bottom with the maximum power labeled with max. All powers are measured at the objective output.

(B) Curves of SBR versus penetration depth for raw data of TPM and mid-NA 2pSAM.

(C) Curves of SBR versus penetration depth for results obtained by TPM with deconvolution and mid-NA 2pSAM. We used n = 50 different images for each depth.

(D) Standard deviation across 500 frames of GCaMP7b imaging results at different depths beneath cortex obtained by TPM and mid-NA 2pSAM. We compared the slice obtained by TPM with and without deconvolution, raw center view of mid-NA 2pSAM, and the reconstructed slice.

(E) Bar plots of the SBR for TPM with and without deconvolution, 2pSAM center view and reconstruction results at different depths (n = 30 sessions for each depth). $^{**}p < 0.01$, $^{***}p < 0.001$. Statistical significance was determined using one-way ANOVA with the Dunnett's multiple comparisons test. We used mean ± standard deviation here.

Scale bars: 100 μm in (A) and (D).

for water-immersion objectives, and imaging through a highly scattering tape (Figure 2F). By decoupling aberration correction from data acquisition, DAO can not only maintain elevated 3D imaging speed with compact systems but also facilitate simultaneous multisite correction of spatially nonuniform aberrations (Video S1, part II). Although resolution and contrast were

Please cite this article in press as: Zhao et al., Two-photon synthetic aperture microscopy for minimally invasive fast 3D imaging of native subcellular behaviors in deep tissue, Cell (2023), https://doi.org/10.1016/j.cell.2023.04.016

CellPress
OPEN ACCESS

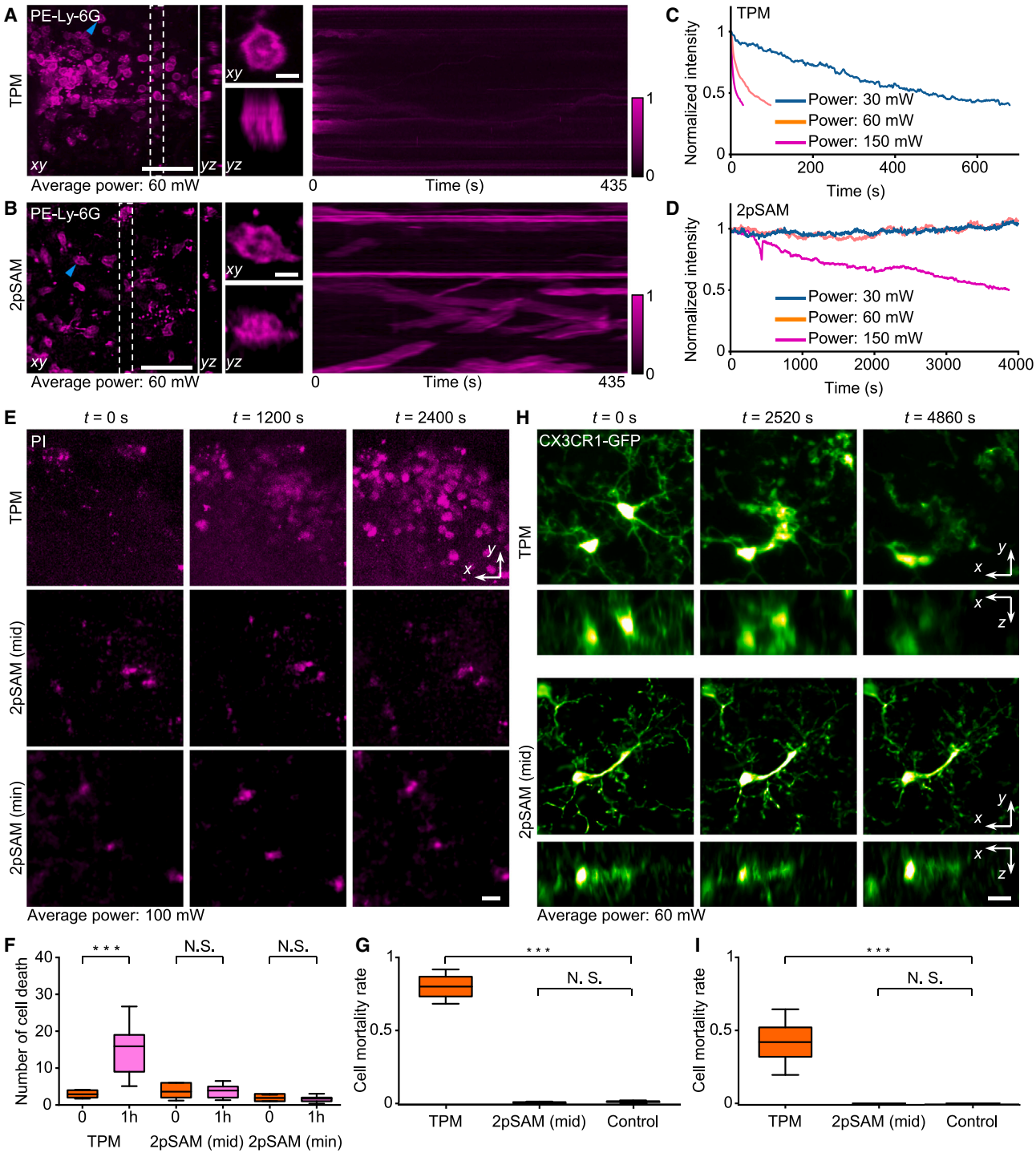

Figure 4. 2pSAM reduces photobleaching and phototoxicity of traditional TPM by orders of magnitude

(A and B) MIPs and kymographs of neutrophils (magenta, PE-Ly-6G) in mice cortex imaged by TPM (A) and 2pSAM (mid) (B). Enlarged orthogonal views correspond to the cells indicated by blue arrows.

(C and D) Curves of normalized average fluorescence intensity versus time in TPM (C) and 2pSAM (D) with the input power of 30, 60, and 150 mW, respectively.

(E) Long-term imaging by TPM and 2pSAM on cells labeled with PI to indicate cell death in mice cortex.

(F) Number of dead cells before and after 1-h continuous imaging by TPM and 2pSAM (n = 10 regions for each).

(G) Bar plots of cell mortality rates during continuous imaging of TPM and 2pSAM on GFP-PI-colabeled B cells *in vitro* under the same power of 50 mW.

(H) Long-term imaging of microglia dynamic in the cortex of CX3CR1-GFP mice by TPM and 2pSAM (mid).

(legend continued on next page)

Please cite this article in press as: Zhao et al., Two-photon synthetic aperture microscopy for minimally invasive fast 3D imaging of native subcellular behaviors in deep tissue, Cell (2023), https://doi.org/10.1016/j.cell.2023.04.016

severely degraded in TPM, 2pSAM well-preserved subcellular structures with high SNR. Since system aberrations can be calibrated in advance, 2pSAM can reduce the costs and sizes of optical systems by orders of magnitude, achieving high-performance imaging in rigorous conditions, such as endoscopy. We show that 2pSAM can increase the imaging performance of a 0.5-NA grin lens implanted in the deep brain of a CX3CR1-GFP mouse with the same power delivered (Figure 2G).

One of the main advantages of two-photon imaging is deep tissue penetration. Therefore, we characterized the penetration capability of 2pSAM by comparing it with TPM at different depths in the same CX3CR1-GFP mouse cortex (Figure 3A). Both raw data and reconstructed results show that 2pSAM has a slightly deeper penetration than TPM in terms of the signal-to-background ratio (SBR; Figures 3B and 3C). Since background fluorescence exhibits different lateral shifts in angular measurements of 2pSAM instead of direct summing up in TPM, these photons far from the native focal plane can be filtered out during 3D deconvolution, akin to computational optical sectioning.[46] Moreover, we imaged calcium dynamics of pyramidal neurons at different cortical layers in virus-infected adult C57BL/6 mice (Figure 3D). Even for a depth of 650 μm, 2pSAM could still readily record neural activities with better SBR than TPM (Figure 3E).

2pSAM reduces phototoxicity during continuous long-term imaging

Although nonlinear two-photon absorption reduces volumetric photobleaching compared with confocal microscopy, extremely high instantaneous local power density raises substantial concerns about the nonlinear phototoxicity interfering with native cellular behaviors.[13,36,37] By comparing TPM and 2pSAM on continuous 3D imaging of different cell types in the mouse cerebral cortex, we find that the accumulated nonlinear photodamage of TPM is underestimated, even for laser powers considerably below the previously characterized power threshold.[47,48] First, we characterized photobleaching *in vivo* by imaging immune cells labeled with PE-Ly-6G in the mice cortical layer 2/3 immediately after craniotomy under different powers (Figures 4A and 4B). 2pSAM can reduce the photobleaching rate of TPM by over 1,000-fold (Figures 4C and 4D; Video S2, part I). An increase of autofluorescence under TPM in tissue was observed with the aggregation of cells labeled with AF488-CD11b after 30 min, whereas cells imaged by 2pSAM behaved naturally (Figure S4A).

To further evaluate phototoxicity, we conducted long-term continuous 3D imaging in cortical layers at a depth of 200 μm to detect phototoxicity-induced apoptotic cells labeled by propidium iodide (PI) (Figure 4E; Video S2, part II). The same power was used to guarantee the same heat damage. The results show that the accumulated nonlinear photodamage led to a significant increase in cell deaths after about 1-h continuous imaging of TPM ($n = 10$; p value < 0.001), whereas 2pSAM shows nearly no phototoxicity (Figure 4F). Then, we conducted an *in vitro* experiment to ensure similar cellularity during comparison by imaging GFP-expressing B cells with PI labeling continuously for an hour with the power of 50 mW (Figure S4B; Video S2, part II). Compared with control experiments (Figure S4C), significant photobleaching and large amounts of additional cell death were observed for TPM with continuous imaging. On the contrary, there was almost no additional cell death for 2pSAM in 6 repeated experiments with about 167-fold reduction in cell mortality, which shows no significant difference compared with the control group (Figure 4G). Furthermore, we labeled GFP-expressing B cells with PE anti-CD86 antibody and found that these immune cells exposed to 2pSAM for more than 7 h remained not activated (Figures S4D–S4G). Consistent phenomena were observed for cellular dynamics in the cortical layer 2/3 of CX3CR1-GFP mice (Figure 4H). We found many microglia dying during continuous imaging of TPM (Figures 4I and S4H). Dynamic extensions and retractions of microglia filopodia were gradually reduced in TPM within half an hour under 60-mW excitation, but behaviors remained similar in 2pSAM (Video S2, part II). All these findings indicate that continuous long-term two-photon imaging with high-NA excitation may disturb normal cellular phenotypes, especially for immune cells. 2pSAM can address this problem and expand practical imaging duration by orders of magnitude.

2pSAM identifies various intercellular communications during TBI

TBI is a major cause of morbidity and disability, with a tremendous socioeconomic burden.[49,50] Following primary injury, a complex cascade of events referred to as secondary injury leads to extensive and sustained damages. However, long-term subcellular interactions among complicated neuroimmune environments are still less understood across multiple scales in the temporal domain due to the limited imaging time window considering phototoxicity. 2pSAM precisely fills this niche.

To analyze the problem, we set up a closed head injury model in mice[51–53] that mirrors some pathological features associated with mild TBI in humans (Figure 5A; STAR Methods). We thinned the murine skull bone to ~30 μm with the underlying meninges and brain parenchyma to be imaged without overt brain injury or inflammation. Under the same imaging conditions, we found that 2pSAM significantly reduced the photobleaching in TPM, elongating the effective imaging durations (Figure S5A). Moreover, we observed that TPM-exposed microglia gradually shrank into spherical structures without filopodia, leading to a significant reduction of cell areas compared with control experiments without continuous imaging (Figures S5B–S5E; Video S3, part I). On the contrary, 2pSAM-exposed microglia maintained active filopodia dynamics, which is critical for intercellular interactions (Figure S5E). 2pSAM showed that acute brain injury induced the generation of many meningeal neutrophils of the peripheral immune system swarming into the parenchyma (Figures 5B and 5C). For comparison, we found that laser-induced injury did not recruit many neutrophils. Although a previous study has visualized rapid microglial process extension after injury, we find that cell bodies of microglia also gradually migrated

(I) Bar plots of cell mortality rate after 90-min continuous imaging of TPM, 2pSAM (mid), and control ($n = 6$ for each). Statistical significance was determined using one-way ANOVA with Dunnett's multiple comparisons tests. N.S., not significant ($p > 0.05$); ***$p < 0.001$. We used mean ± standard deviation here.
Scale bars: 50 μm and 5 μm (for zoom-in views) in (A) and (B) and 10 μm in (E) and (H). See also Figure S4.

Please cite this article in press as: Zhao et al., Two-photon synthetic aperture microscopy for minimally invasive fast 3D imaging of native subcellular behaviors in deep tissue, Cell (2023), https://doi.org/10.1016/j.cell.2023.04.016

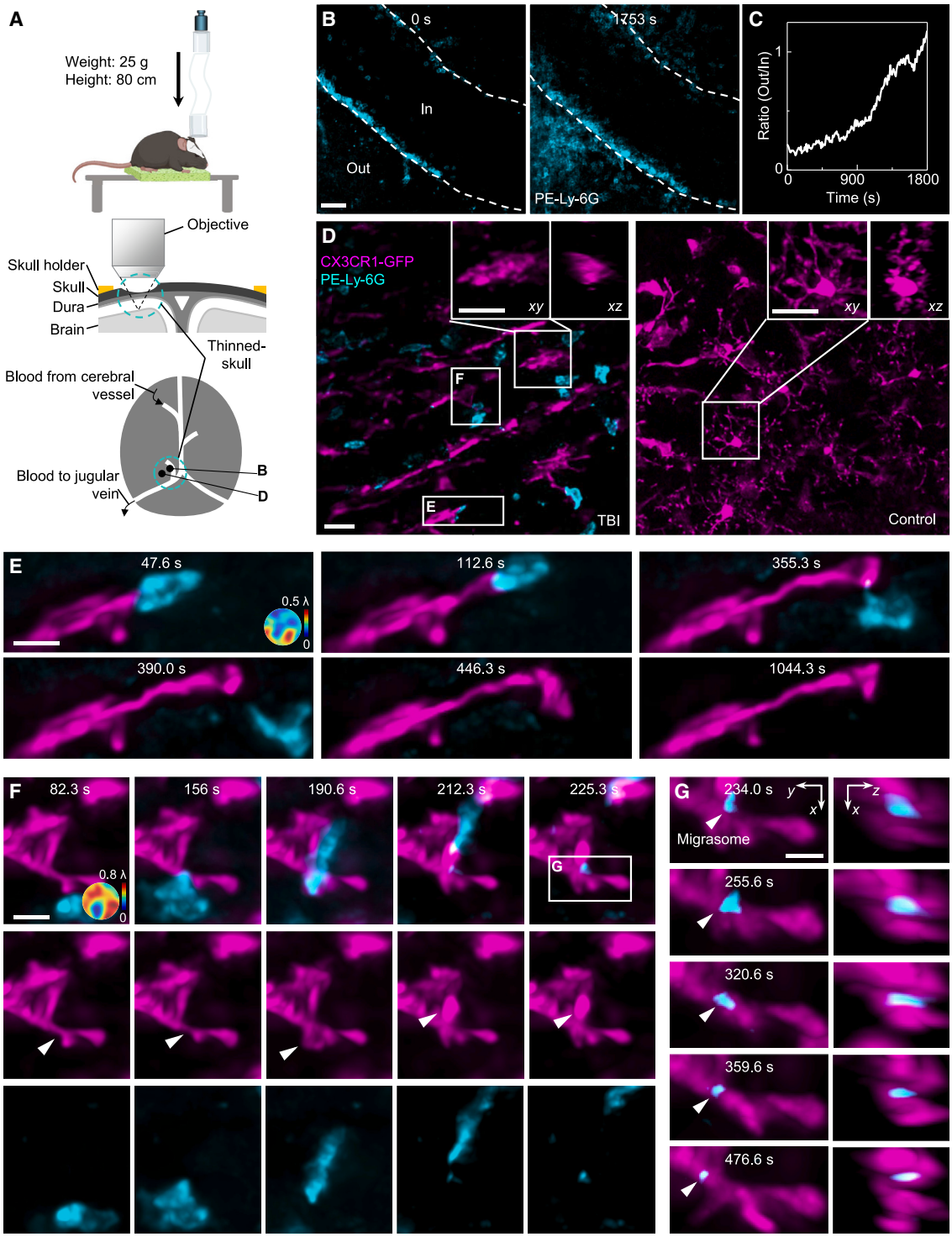

Figure 5. 2pSAM visualizes diverse subcellular interactions between peripheral and central immune systems following TBI

(A) Illustrations of TBI imaging model. Blue dashed circles demonstrate imaged anatomical sites in mice cortex.

(B) Neutrophils (blue, PE-Ly-6G) swarmed into parenchyma from blood vessels following TBI. Dashed lines mark the vessel margin.

(C) Curve of average ratio between numbers of neutrophils in parenchyma and vessels versus time.

(D) Large-scale interactions between neutrophils (blue, Ly-6G) and CX3CR1-positive microglia/macrophages/monocytes that follows TBI (left). In the non-TBI control, virtually no such interaction has been observed (right).

(E) A neutrophil pulled one microglia to stretch following TBI.

(legend continued on next page)

Please cite this article in press as: Zhao et al., Two-photon synthetic aperture microscopy for minimally invasive fast 3D imaging of native subcellular behaviors in deep tissue, Cell (2023), https://doi.org/10.1016/j.cell.2023.04.016

to the damaged spot at low speed across several hours (Figures S5F–S5I; Video S3, part II). Various interactions between PE-Ly-6G-labeled neutrophils and CX3CR1-positive microglia/macrophages/monocytes were observed in the central nervous microenvironment (Figures 5D and 5E; Video S4). We find that the neutrophil moved rapidly to the microglia and produced migrasomes[5,54,55] after the generation of retraction fibers by directly adhering to the microglia (Figure 5F). There was fluorescence enrichment in microglia with a protrusion during migrasome generation. By monitoring over a long term, the migrasome was then picked up by the microglia and transported to be phagocytosed indicated by 3D information (Figure 5G). As an organelle,[56] the migrasome has shown multiple functions such as regional cues for organ morphogenesis,[57,58] mitocytosis,[58] and angiogenesis[59] but has barely been studied in the mammalian brain due to scattering environments and organelle sensitivity to light doses.[54] Such native subcellular dynamics observed by 2pSAM indicate that neutrophils in the peripheral immune system may deliver signals directly to specific immune cells in the central nervous system through complex interactions such as contact-generated migrasomes or pulling processes to enhance the neuroimmune surveillance system. Targeting these migrasome formation and pulling processes may offer fresh insights for developing effective TBI therapies.

Progression of GC formation visualized by 2pSAM

GCs are dynamic tissue microdomains in secondary lymphoid organs, where T and B lymphocytes collaborate to support the generation of long-lived plasma cells and memory B cells.[60] Following immunization, the GC structure emerges in the center of the lymphoid follicles as antigen-activated B cells are directed by chemo-attractants to congregate. Static and dynamic imaging have recorded dynamic behaviors of B cells during different stages of B cell responses *in vivo*.[61] However, due to stochastic behaviors of GC initiation and photosensitivity of immune cells, a complete initial GC formation process has not been visualized at high speed.

We chose to image the inguinal lymph node, which was extensively used to understand B cell dynamics.[8,62] With multi-view information, 2pSAM allowed real-time depth estimation during imaging, which was used as the feedback for adjusting objective positions to achieve automatic focusing across several hours (Figure S6A) and compensate focal drifts during immune responses (Figure S6B; Video S5, part I). Preliminary analysis showed that in the MD4/OT-II co-transfer system, histologically identifiable GC clusters typically began to form 96 h after immunization. We therefore conducted 2pSAM imaging from 90 to 110 h post-immunization to record the whole GC formation process by sparsely labeling 4% of the total responding cells at high speed for single-cell tracking (Figure 6A; Video S5, part II). By comparing TPM with 2pSAM under the same condition, we found that there was more severe photobleaching in TPM, restricting the effective imaging durations (Figure S6C). More importantly, continuous exposure to TPM results in abnormal behaviors of B cells indicated by the significantly reduced cell motilities (Figure S6D). Such strongly accumulated phototoxicity has also been verified in *in vitro* experiments of isolated B cells (Figure 4G). Therefore, it has long been a challenge for TPM to document this critical event of the initial GC formation. 2pSAM serves as an ideal method to address these problems by continuously imaging a large tissue volume at a high spatiotemporal resolution over a prolonged period of time with minimal phototoxicity and the ability to accommodate and adapt to morphological changes of lymphoid tissue during immune responses.

Then, we tracked individual cells of sparsely labeled cohorts to characterize GC formation dynamics by 2pSAM (Figures 6B and 6C). By monitoring cell densities in the locale of the eventual GC cluster, we could observe a phase of moderate accumulation followed by a phase of rapid accumulation (Figure 6D). This phase transition, reminiscent of the replica symmetry breaking in complex systems,[63] was accompanied by a relatively sharp reduction of the average migration speed (Figures 6E and S6E). Consistent with the increase in the cell density in the GC locale, distances between cells decreased in the GC region over time (Figure 6F; other examples are shown in Figures S6F–S6H). Then, we studied whether the initial GC formation was mainly due to the recruitment and congregation of cells in a narrow volume or due to the proliferative cell expansion. As shown in Figure 6G, there was a steady net flow of sparsely labeled cells into the GC locale but not to a similar non-GC locale. On the other hand, the increase of total cells markedly outstripped the net inflow, with the difference being accountable only by cell proliferation in the locale (Figure 6H). This local proliferation sharply increased at around 6 h during imaging, approximately coinciding with the sudden cell-density increase. These data indicate the initial GC formation, characterized by a phase transition-like sudden clustering, mainly resulted from the rapid proliferation of a smaller number of recruited B cells.

In additional detailed analyses of the cell traces over the long term, incoming B cells that located outside of the GC-forming region showed disadvantages in locating in the center of the GC region (Figure 6I), suggesting the compromised capacity of participating in the GC reaction. Within the period of observation, although in the non-GC region, the traces of incoming B cells were approximately evenly distributed in the outer region or the non-GC region or the interface region, in the GC-forming region, most traces of incoming B cells were stuck in the GC-interface region or the outer region (Figures S6I and S6J). Collectively, our data suggest that through a tissue-scale phase-transition-like process, GCs initially come to be the densely packed dynamic structure by a proliferative burst of B cells, rather than by the continuous recruitment of large numbers of cells from outside. In the future, long-term high-speed 3D imaging by 2pSAM will facilitate more holistic analyses of GC formation and development, with all intricate details of cell-cell interactions, in a completely spatiotemporally resolved manner.

(F) A neutrophil generates migrasome through direct contact with microglia following TBI. Fluorescence enrichment (marked by white arrows) in the microglia with a protrusion was observed during migrasome generation.
(G) Migrasome generated during direct contact was then sent into the microglia indicated by 3D visualizations.
Scale bars: 40 μm in (B); 20 μm in (D); 10 μm in (E) and (F); and 5 μm in (G). See also Figure S5.

Please cite this article in press as: Zhao et al., Two-photon synthetic aperture microscopy for minimally invasive fast 3D imaging of native subcellular behaviors in deep tissue, Cell (2023), https://doi.org/10.1016/j.cell.2023.04.016

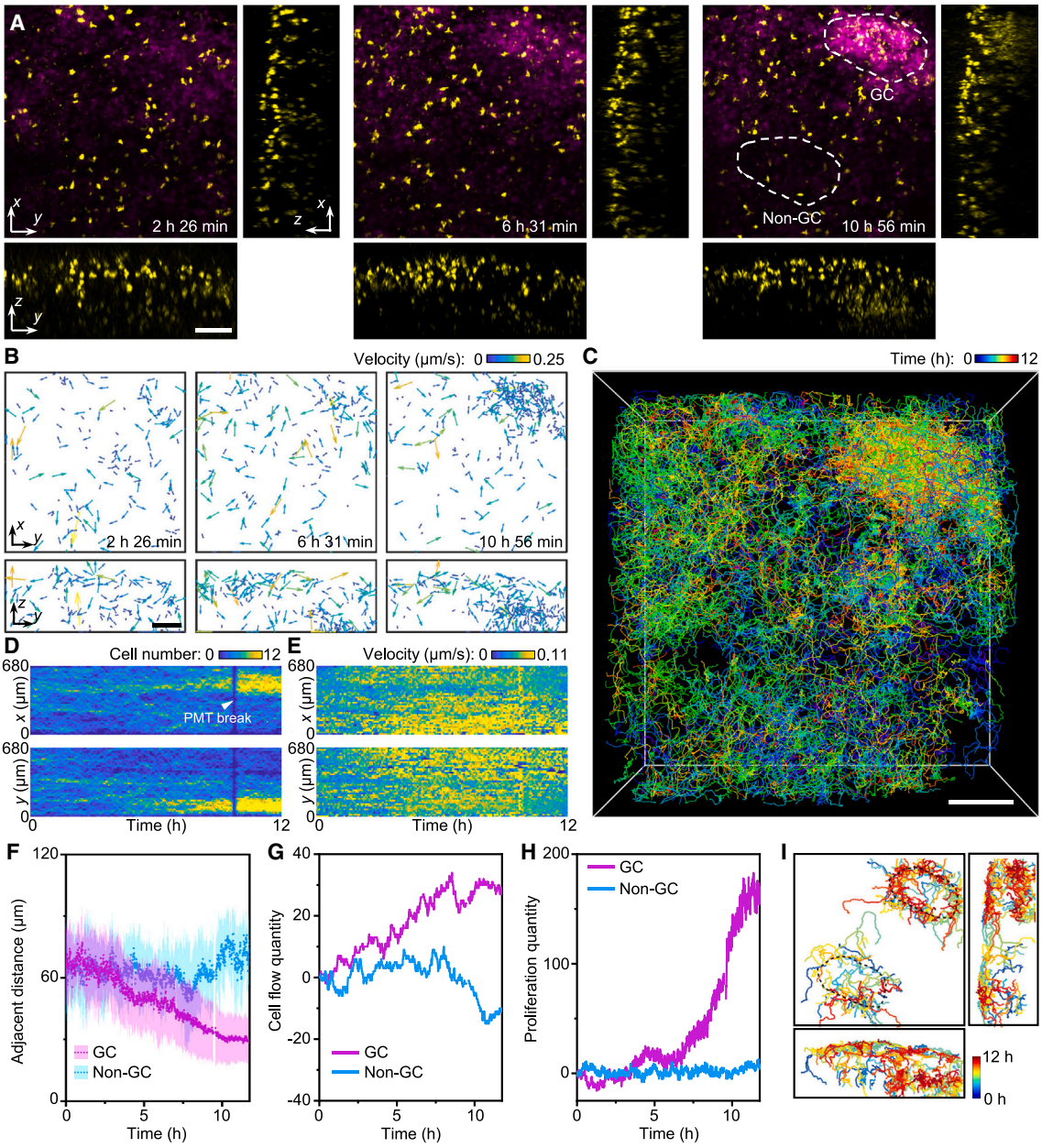

Figure 6. System dynamics during progression of GC formation observed by 2pSAM

(A) Recording of complete GC formation process for up to 12 h at high speed in a mouse lymph node *in vivo* (Video S5, part II). Yellow channel marks sparse B cells for tracking and analyzing, whereas magenta channel marks dense B cells, highlighting the size and location of GC.

(B) Velocities of tracked cells at three time points during GC formation indicated by color-coded arrows.

(C) Overlay of tracked traces across the whole process in 3D.

(D and E) Map of average local cell densities (D) and velocities (E) along the *x* and *y* directions.

(F) Curves of adjacent distances between cells versus time for the GC region (magenta) and the non-GC region (blue) marked in (A).

(G) Curves of cell flow quantity (number of cells flowing into the region) versus time for the GC and non-GC regions. Negative values mean flowing out.

(H) Curves of proliferation quantity of cells in the GC and non-GC regions.

(I) Traces of cells crossing through the GC and non-GC regions.

Scale bars: 100 μm in (A)–(C). See also Figure S6.

Please cite this article in press as: Zhao et al., Two-photon synthetic aperture microscopy for minimally invasive fast 3D imaging of native subcellular behaviors in deep tissue, Cell (2023), https://doi.org/10.1016/j.cell.2023.04.016

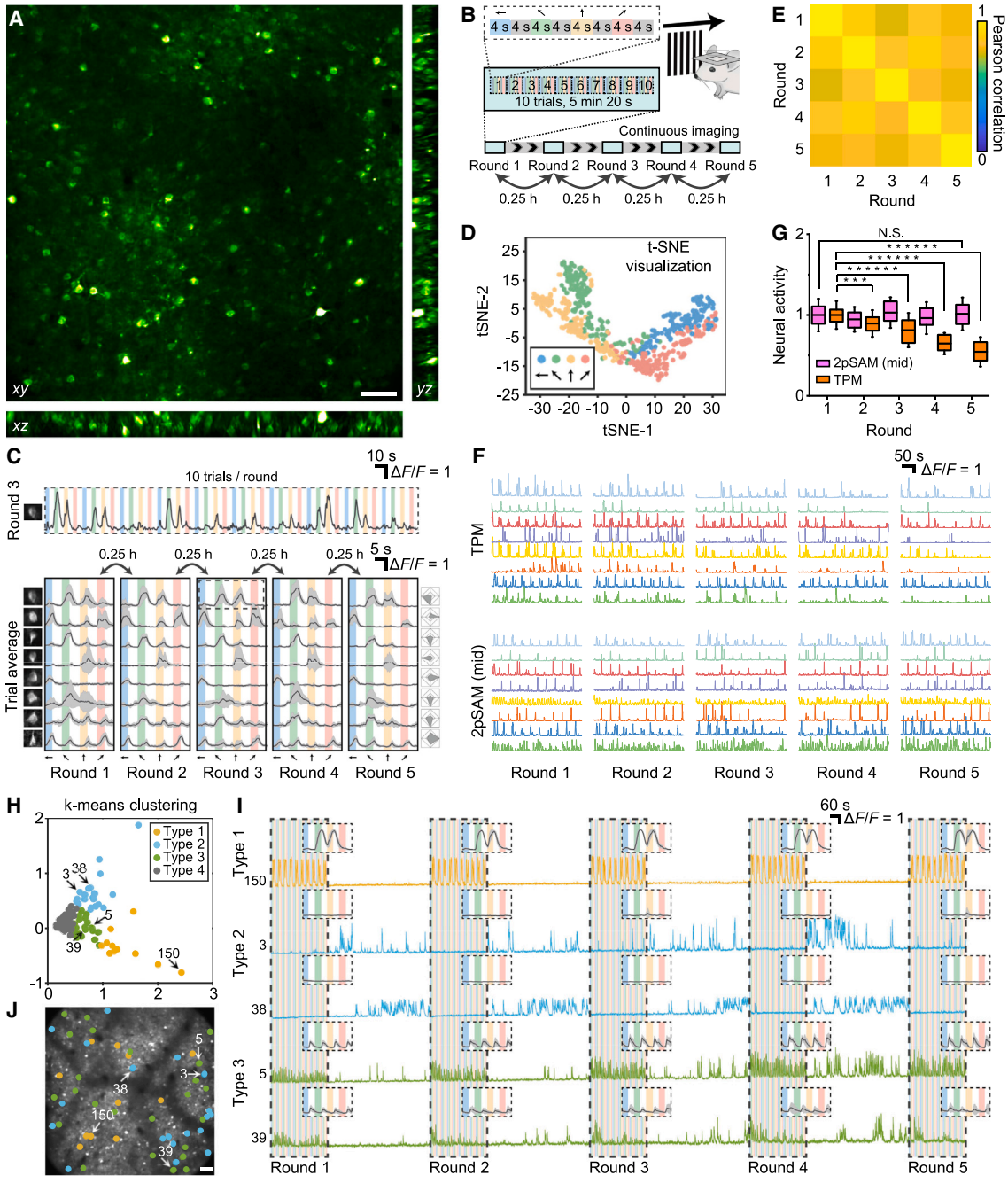

Figure 7. Long-term high-speed neural recording by 2pSAM with reduced phototoxicity reveals heterogeneous cellular states

(A) Orthogonal MIPs of standard deviations of volumes obtained by mid-NA 2pSAM in the V1 cortex of head-fixed Rasgrf2-2A-dCre;Ai148d mice (Video S6).

(B) Schematic of long-term repeated visual stimulus.

(C) Representative neurons with stable responses to different directions of moving gratings. Both single-round traces and trial-average traces of different rounds are shown.

(D) Dimensionality reduction (t-distributed stochastic neighbor embedding [tSNE]) applied to extracted temporal traces in (C). Each point corresponds to neural activities during the period of one direction.

(E) Correlation map of trial-average neural activities among different rounds.

(F) Representative traces obtained by TPM and mid-NA 2pSAM under the same condition.

(G) Bar plots of averaged neural activities responding to visual stimulus by TPM and 2pSAM (mid). N = 3 different mice, each with 20 neurons.

(H) k-means clustering of neurons responding to visual stimuli with 4 types.

(legend continued on next page)

Please cite this article in press as: Zhao et al., Two-photon synthetic aperture microscopy for minimally invasive fast 3D imaging of native subcellular behaviors in deep tissue, Cell (2023), https://doi.org/10.1016/j.cell.2023.04.016

Long-term high-speed 3D neural recording reveals heterogeneous cellular states

Neural activities are remarkably plastic, adapting to the changes in internal states and salient environmental cues.[64,65] However, it remains unclear how neural dynamics of the same neuron change at different stages lasting for hours and the extent to which different types of neurons in the same region follow the same rules. 2pSAM provides the opportunity to capture rapid transitions between cellular states in long-term dynamic scenarios and characterize different neural identities.

We conducted calcium imaging in the V1 region of head-fixed Rasgrf2-2A-dCre;Ai148d mice with comparisons between TPM and 2pSAM (Figures 7A, S7A, and S7B) and analyzed the stability of visual representations on hour-long continuous high-speed imaging. We gave mice 5 rounds of visual stimulus, with each round consisting of 10 trials and the round interval of 15 min, and imaged their V1 regions continuously during the whole process (Video S6). Each trial includes moving gratings of four different angles with intervals of 8 s for every direction (Figure 7B; STAR Methods).

With mid-NA 2pSAM, we found that neurons had very stable responses to specific visual stimuli across an hour (Figure 7C). The temporal traces during stimulus can be clustered into four classes corresponding to four angles (Figure 7D). In addition, the activity patterns responding to the visual stimulus were highly correlated among different rounds across an hour (Figure 7E). Moreover, in all these cases, 2pSAM maintained a similar strength of neural activities over an hour, whereas the average strength of neural activities in TPM rapidly decreased (Figures 7F and 7G). The same phenomena could be repeatedly observed in different mice (Figure S7C). If we further increased the laser power to 200 mW, the decrease in neural activities happened earlier (Figure S7D). These observations indicate that neural responses under visual stimulus including both tuning curves and average firing rates in the visual cortex are both stable over hour-long timescales. More attention should be paid when applying traditional TPM in long-term continuous neural recording, since the native neural activities can be influenced by nonlinear photodamage with only 100 mW in layer 2/3 of the mice cortex.

Closer examinations of the complete traces obtained by 2pSAM using k-means clustering revealed four dominant response types and uncovered a continuum of neural states across the hour-long visual task (Figure 7H). Except for the neural types responding to the visual stimuli mentioned above (type 1), we found other distinct cell types, which were rapidly suppressed by visual stimulus and elevated during gray screen without gratings (Figures 7I and S7E). Specifically, one type of neuron (type 2) was very active in the between-round gray screen period but silent within each round. Another type of neuron (type 3) responded both in the between-round and between-stimulus gray screen intervals but was inactive during the visual stimulus. In addition, between-round spontaneous activities of these type 3 neurons gradually increased across the whole experimental procedure. In this regard, type 2 and type 3 neurons may encode states of resting and visual habituation, respectively. Besides, all of these types of neurons are distributed in the pattern of salt and pepper (Figure 7J). Taken together, when adapting to changes in internal states and salient environmental cues, stable visual-evoked and dynamic heterogeneous spontaneous activities may work simultaneously to facilitate the constancy and plasticity of visual recognition and perception.

DISCUSSION

Although advanced light-sheet microscopy and light-field microscopy have recently realized long-term high-speed 3D imaging of subcellular structures in weakly scattering specimens,[5,32] such a capability in deep tissue remains an unmet requirement, restricting broad applications in life science where most important anatomical structures are embedded in the tissue such as the blood–brain barrier, GC, and neurons in deep cortical layers. 2pSAM exactly fills this niche. Different from scanning light-field microscopy with a drifting microlens array for the wide-field detection of spatial-angular measurements,[5] 2pSAM scans needle-like beams across the 2D spatial and 2D angular domains for two-photon excitation, which provides a computational solution to high-speed 3D imaging of subcellular dynamics with much deeper penetration depth than one-photon imaging methods (Figure 3). A pinhole is added to introduce the spatial constraint for aperture synthesis close to the diffraction limit of whole-objective NA, enabling multisite aberration correction at high speed with low cost and compact systems (Figure 2G). Rather than collecting more effective photons in the extended DOF, 2pSAM achieves extremely low phototoxicity by reducing the peak laser power with similar fluorescence outcomes (Figure 4). Together with the motion correction and autofocus algorithms, 2pSAM facilitates diverse studies of intercellular dynamics and interactions in the native microenvironment across multiple temporal scales. Only simple modifications with a compact add-on can convert a traditional TPM into 2pSAM (Figure S1). Moreover, 2pSAM is compatible with most existing image-enhancement algorithms. With the DeepCAD denoising method,[66,67] large-scale 3D neural recording at 30 volume/s was obtained with an extremely low power of about 5 mW, leading to further longer imaging durations (Figures S7F and S7G). We can also explore the spatio-temporal sparse prior in neural activities to increase the SNR by simply using standard deviations as the initial value during reconstruction (Figures S7H and S7I).

(I) Several examples of 3 different neuron types, including visual stimulus excitatory neurons (type 1), and visual stimulus inhibited neurons (type 2 and type 3). Type 2 neurons were mainly active in-between round gray screen period, while type 3 neurons responded both in-between round and between-trial intervals without responses during visual stimulus. Trial-average of each round is displayed at the top-right corner.

(J) Spatial distribution of three types of neurons of interest. Statistical significance was determined using one-way ANOVA with the Dunnett's multiple comparisons test. N.S., not significant ($p > 0.05$); ***$p < 0.001$, ******$p < 0.000001$. We used mean ± standard deviation here.

Scale bars: 50 μm in (A) and (J). See also Figure S7.

We have demonstrated several exemplar applications in pathology (Figure 5), immunology (Figure 6), and neuroscience (Figure 7), which are challenging for previous methods. These are only the tip of the iceberg, and many more applications can be exploited. For example, we found that continuous 3D imaging by TPM resulted in severe damages to *Drosophila* embryos. On the contrary, using the same laser power, 2pSAM could continuously record the entire process over 17 h at a high 3D imaging speed with a much higher hatching rate, indicating its great potential in developmental biology (Video S2, part III). Moreover, biological tissues are built from the ensembles of heterogeneous cells in different states. Capturing the transient cellular or subcellular dynamics and interactions across multiple pathological or physiological states with 2pSAM, together with advanced spatial transcriptomics technology,[16,68] offer great opportunities to better understand how living systems organize and respond to different stimuli within an extended time window, such as the cellular states, organizations and functions of neural circuits,[15,69] immune responses,[14] neuroinflammation,[53,70] neurodegenerative disorders,[71] and tumorigenesis.[72]

Limitations of the study

Although conventional TPM has the same resolution at different planes with axial scanning, the resolution of 2pSAM gradually decreases with the increase of the distance from the native objective plane. Such a nonuniform resolution reduces the contrast of high-frequency components such as neural synapses in the maximum intensity projection (MIP). Multifocus excitation[73] or deep learning-based algorithms[74,75] can be exploited in the future to achieve 3D reconstructions with uniform resolutions. In the meantime, as each sampling point in 2pSAM is the multiplexing of multiple voxels in TPM, the SNR of weak signals may be reduced with the existence of a very bright point due to the limited dynamic range of detectors (16 bits here). For the motion-correction algorithm, we have quantitatively evaluated the correction performance with different motion speeds (Figures S3A–S3E). More iteration numbers are required for highly dynamic samples, otherwise, there will be motion artifacts after reconstruction (Figure S3E). For multisite aberration corrections, we assume that aberrations change smoothly within the whole FOV. Otherwise, the FOV needs to be divided into smaller tiles during reconstruction with larger computational costs and reduced accuracy of aberration estimation. For 3D reconstruction, 2pSAM requires an iterative reconstruction to obtain aberration-corrected high-resolution volumes. As a tomographic imaging method sampling in the k-space domain like X-ray computed tomography, the resolution of 2pSAM will decrease for very dense samples with a fixed number of angles (Figures S2F–S2I). More angles are required for dense samples at the cost of net imaging speed especially for 2pSAM with a smaller sub-aperture NA covering a larger DOF, corresponding to a smaller coverage in the k-space domain. Our results show that 13 angles are saturated for mid-NA 2pSAM (Figure S2G). Learning-based algorithms can be applied in the future to reduce the computational costs and required angle numbers.[74,75] Finally, more advanced downstream analysis algorithms should be developed to handle huge amounts of data.

STAR★METHODS

Detailed methods are provided in the online version of this paper and include the following:

- KEY RESOURCES TABLE
- RESOURCE AVAILABILITY
  - Lead contact
  - Materials availability
  - Data and code availability
- EXPERIMENTAL MODEL AND SUBJECT DETAILS
  - Animals
  - *In vitro* experiments of cell death and activation
  - *Drosophila* embryos
  - Mouse TBI model
  - Laser-induced injury imaging
  - Lymph node imaging
  - Neural imaging
  - Evaluation of 2pSAM on different wavelengths
  - Slice preparation
- METHOD DETAILS
  - Experimental setup
  - 3D reconstruction algorithm with DAO
  - System calibration
  - Motion correction with a sliding window
  - Numerical simulation
  - Mouse experiments
  - Immune cell imaging in cortex
  - Detection of dead or activated cells
- QUANTIFICATION AND STATISTICAL ANALYSIS
  - Image analysis
  - Calcium imaging analysis
  - Cell tracking
  - SBR calculation
  - Cell death
  - Statistical analysis

SUPPLEMENTAL INFORMATION

Supplemental information can be found online at https://doi.org/10.1016/j.cell.2023.04.016.

ACKNOWLEDGMENTS

We thank Jiaqi Fan for her assistance in *Drosophila* preparation and Yi Zhang and Yuduo Guo for helpful discussion. We would like to acknowledge the assistance of the Imaging Core Facility, Technology Center for Protein Sciences, Tsinghua University for assistance of using Imaris 9.3. Z.Z., Y.Z., J.H., Y.C., J.F., X.L., J.Z., Z.W., Z.L., J.W., and Q.D. were supported by National Natural Science Foundation of China (61927802, 62088102, 62222508, 62071272) and Beijing Natural Science Foundation (JQ21012). B.L. and H.Q. were funded by National Natural Science Foundation of China (81621002).

AUTHOR CONTRIBUTIONS

Conceptualization, J.W.; methodology, Z.Z., J.W., B.L., J.H., and Y.Z.; software, J.W., Y.Z., and Z.Z.; validation of methods, J.W. and J.F.; validation of biological experiments, H.Q.; formal analysis, Z.Z., Y.Z., B.L., J.H., and J.W.; investigation, Z.Z., Y.Z., B.L., J.H., J.W., X.L., Z.W., and J.Z.; resources, Q.D., J.W., and H.Q.; visualization, Z.Z., Y.Z., J.Z., Y.C., Z.L., and J.F.; funding

acquisition, Q.D., H.Q., J.W., and J.F.; project administration, J.W. and Q.D.; supervision, Q.D., H.Q., and J.W.; writing, J.W., Z.Z., B.L., J.H., H.Q., and Q.D.

DECLARATION OF INTERESTS

Q.D., J.F., and J.W. are founders and equity holders of Zhejiang Hehu Technology LLC. Q.D., J.W., Z.Z., Y.Z., and J.F. submitted patent applications related to the 2pSAM method developed in this work.

INCLUSION AND DIVERSITY

We support inclusive, diverse, and equitable conduct of research.

Received: November 2, 2022
Revised: February 21, 2023
Accepted: April 10, 2023
Published: May 12, 2023

REFERENCES

1. Kitching, A.R., and Hickey, M.J. (2022). Immune cell behaviour and dynamics in the kidney - insights from in vivo imaging. Nat. Rev. Nephrol. *18*, 22–37. https://doi.org/10.1038/s41581-021-00481-9.
2. Hor, J.L., and Germain, R.N. (2022). Intravital and high-content multiplex imaging of the immune system. Trends Cell Biol. *32*, 406–420. https://doi.org/10.1016/j.tcb.2021.11.007.
3. Yang, W., and Yuste, R. (2017). In vivo imaging of neural activity. Nat. Methods *14*, 349–359. https://doi.org/10.1038/nmeth.4230.
4. Parkhurst, C.N., Yang, G., Ninan, I., Savas, J.N., Yates, J.R., 3rd, Lafaille, J.J., Hempstead, B.L., Littman, D.R., and Gan, W.B. (2013). Microglia promote learning-dependent synapse formation through brain-derived neurotrophic factor. Cell *155*, 1596–1609. https://doi.org/10.1016/j.cell.2013.11.030.
5. Wu, J., Lu, Z., Jiang, D., Guo, Y., Qiao, H., Zhang, Y., Zhu, T., Cai, Y., Zhang, X., Zhanghao, K., et al. (2021). Iterative tomography with digital adaptive optics permits hour-long intravital observation of 3D subcellular dynamics at millisecond scale. Cell *184*, 3318–3332.e17. https://doi.org/10.1016/j.cell.2021.04.029.
6. Huang, Q., Cohen, M.A., Alsina, F.C., Devlin, G., Garrett, A., McKey, J., Havlik, P., Rakhilin, N., Wang, E., Xiang, K., et al. (2020). Intravital imaging of mouse embryos. Science *368*, 181–186. https://doi.org/10.1126/science.aba0210.
7. Denk, W., Strickler, J.H., and Webb, W.W. (1990). Two-photon laser scanning fluorescence microscopy. Science *248*, 73–76. https://doi.org/10.1126/science.2321027.
8. Liu, B., Lin, Y., Yan, J., Yao, J., Liu, D., Ma, W., Wang, J., Liu, W., Wang, C., Zhang, L., and Qi, H. (2021). Affinity-coupled CCL22 promotes positive selection in germinal centres. Nature *592*, 133–137. https://doi.org/10.1038/s41586-021-03239-2.
9. Cahalan, M.D., Parker, I., Wei, S.H., and Miller, M.J. (2002). Two-photon tissue imaging: seeing the immune system in a fresh light. Nat. Rev. Immunol. *2*, 872–880. https://doi.org/10.1038/nri935.
10. Wu, J., Ji, N., and Tsia, K.K. (2021). Speed scaling in multiphoton fluorescence microscopy. Nat. Photonics *15*, 800–812. https://doi.org/10.1038/s41566-021-00881-0.
11. Hampson, K.M., Turcotte, R., Miller, D.T., Kurokawa, K., Males, J.R., Ji, N., and Booth, M.J. (2021). Adaptive optics for high-resolution imaging. Nat. Rev. Methods Primers *1*, 68. https://doi.org/10.1038/s43586-021-00066-7.
12. Pittet, M.J., and Weissleder, R. (2011). Intravital imaging. Cell *147*, 983–991. https://doi.org/10.1016/j.cell.2011.11.004.
13. Ji, N., Magee, J.C., and Betzig, E. (2008). High-speed, low-photodamage nonlinear imaging using passive pulse splitters. Nat. Methods *5*, 197–202. https://doi.org/10.1038/nmeth.1175.
14. Pittet, M.J., Garris, C.S., Arlauckas, S.P., and Weissleder, R. (2018). Recording the wild lives of immune cells. Sci. Immunol. *3*, eaaq0491. https://doi.org/10.1126/sciimmunol.aaq0491.
15. Kasai, H., Ziv, N.E., Okazaki, H., Yagishita, S., and Toyoizumi, T. (2021). Spine dynamics in the brain, mental disorders and artificial neural networks. Nat. Rev. Neurosci. *22*, 407–422. https://doi.org/10.1038/s41583-021-00467-3.
16. Crainiciuc, G., Palomino-Segura, M., Molina-Moreno, M., Sicilia, J., Aragones, D.G., Li, J.L.Y., Madurga, R., Adrover, J.M., Aroca-Crevillén, A., Martin-Salamanca, S., et al. (2022). Behavioural immune landscapes of inflammation. Nature *601*, 415–421. https://doi.org/10.1038/s41586-021-04263-y.
17. Tanay, A., and Regev, A. (2017). Scaling single-cell genomics from phenomenology to mechanism. Nature *541*, 331–338. https://doi.org/10.1038/nature21350.
18. Papagiakoumou, E., Ronzitti, E., and Emiliani, V. (2020). Scanless two-photon excitation with temporal focusing. Nat. Methods *17*, 571–581. https://doi.org/10.1038/s41592-020-0795-y.
19. Yang, W., Miller, J.E., Carrillo-Reid, L., Pnevmatikakis, E., Paninski, L., Yuste, R., and Peterka, D.S. (2016). Simultaneous multi-plane imaging of neural circuits. Neuron *89*, 269–284. https://doi.org/10.1016/j.neuron.2015.12.012.
20. Demas, J., Manley, J., Tejera, F., Barber, K., Kim, H., Traub, F.M., Chen, B., and Vaziri, A. (2021). High-speed, cortex-wide volumetric recording of neuroactivity at cellular resolution using light beads microscopy. Nat. Methods *18*, 1103–1111. https://doi.org/10.1038/s41592-021-01239-8.
21. Beaulieu, D.R., Davison, I.G., Kılıç, K., Bifano, T.G., and Mertz, J. (2020). Simultaneous multiplane imaging with reverberation two-photon microscopy. Nat. Methods *17*, 283–286. https://doi.org/10.1038/s41592-019-0728-9.
22. Wu, J., Liang, Y., Chen, S., Hsu, C.L., Chavarha, M., Evans, S.W., Shi, D., Lin, M.Z., Tsia, K.K., and Ji, N. (2020). Kilohertz two-photon fluorescence microscopy imaging of neural activity in vivo. Nat. Methods *17*, 287–290. https://doi.org/10.1038/s41592-020-0762-7.
23. Wang, J., Hua, X., Guo, C., Liu, W., and Jia, S. (2020). Airy-beam tomographic microscopy. Optica *7*, 790–793. https://doi.org/10.1364/optica.389894.
24. He, H., Kong, C., Tan, X.J., Chan, K.Y., Ren, Y.X., Tsia, K.K., and Wong, K.K.Y. (2019). Depth-resolved volumetric two-photon microscopy based on dual Airy beam scanning. Opt. Lett. *44*, 5238–5241. https://doi.org/10.1364/OL.44.005238.
25. Kazemipour, A., Novak, O., Flickinger, D., Marvin, J.S., Abdelfattah, A.S., King, J., Borden, P.M., Kim, J.J., Al-Abdullatif, S.H., Deal, P.E., et al. (2019). Kilohertz frame-rate two-photon tomography. Nat. Methods *16*, 778–786. https://doi.org/10.1038/s41592-019-0493-9.
26. Song, A., Charles, A.S., Koay, S.A., Gauthier, J.L., Thiberge, S.Y., Pillow, J.W., and Tank, D.W. (2017). Volumetric two-photon imaging of neurons using stereoscopy (vTwINS). Nat. Methods *14*, 420–426. https://doi.org/10.1038/nmeth.4226.
27. Akemann, W., Wolf, S., Villette, V., Mathieu, B., Tangara, A., Fodor, J., Ventalon, C., Léger, J.F., Dieudonné, S., and Bourdieu, L. (2022). Fast optical recording of neuronal activity by three-dimensional custom-access serial holography. Nat. Methods *19*, 100–110. https://doi.org/10.1038/s41592-021-01329-7.
28. Chen, W., Natan, R.G., Yang, Y., Chou, S.W., Zhang, Q., Isacoff, E.Y., and Ji, N. (2021). In vivo volumetric imaging of calcium and glutamate activity at synapses with high spatiotemporal resolution. Nat. Commun. *12*, 6630. https://doi.org/10.1038/s41467-021-26965-7.
29. Lu, R., Sun, W., Liang, Y., Kerlin, A., Bierfeld, J., Seelig, J.D., Wilson, D.E., Scholl, B., Mohar, B., Tanimoto, M., et al. (2017). Video-rate volumetric functional imaging of the brain at synaptic resolution. Nat. Neurosci. *20*, 620–628. https://doi.org/10.1038/nn.4516.

30. Zheng, W., Wu, Y., Winter, P., Fischer, R., Nogare, D.D., Hong, A., McCormick, C., Christensen, R., Dempsey, W.P., Arnold, D.B., et al. (2017). Adaptive optics improves multiphoton super-resolution imaging. Nat. Methods *14*, 869–872. https://doi.org/10.1038/nmeth.4337.

31. Park, J.H., Kong, L., Zhou, Y., and Cui, M. (2017). Large-field-of-view imaging by multi-pupil adaptive optics. Nat. Methods *14*, 581–583. https://doi.org/10.1038/nmeth.4290.

32. Liu, T.L., Upadhyayula, S., Milkie, D.E., Singh, V., Wang, K., Swinburne, I.A., Mosaliganti, K.R., Collins, Z.M., Hiscock, T.W., Shea, J., et al. (2018). Observing the cell in its native state: imaging subcellular dynamics in multicellular organisms. Science *360*, eaaq1392. https://doi.org/10.1126/science.aaq1392.

33. Moreira, A., Prats-Iraola, P., Younis, M., Krieger, G., Hajnsek, I., and Papathanassiou, K.P. (2013). A tutorial on synthetic aperture radar. IEEE Geosci. Remote Sens. Mag. *1*, 6–43. https://doi.org/10.1109/MGRS.2013.2248301.

34. Stelzer, E.H.K., Strobl, F., Chang, B.-J., Preusser, F., Preibisch, S., McDole, K., and Fiolka, R. (2021). Light sheet fluorescence microscopy. Nat. Rev. Methods Primers *1*, 73. https://doi.org/10.1038/s43586-021-00069-4.

35. Levoy, M., Ng, R., Adams, A., Footer, M., and Horowitz, M. (2006). Light field microscopy. ACM Trans. Graphics *25*, 924–934. https://doi.org/10.1145/1141911.1141976.

36. Patterson, G.H., and Piston, D.W. (2000). Photobleaching in two-photon excitation microscopy. Biophys. J. *78*, 2159–2162. https://doi.org/10.1016/S0006-3495(00)76762-2.

37. Hopt, A., and Neher, E. (2001). Highly nonlinear photodamage in two-photon fluorescence microscopy. Biophys. J. *80*, 2029–2036. https://doi.org/10.1016/S0006-3495(01)76173-5.

38. Singh, A., McMullen, J.D., Doris, E.A., and Zipfel, W.R. (2015). Comparison of objective lenses for multiphoton microscopy in turbid samples. Biomed. Opt. Express *6*, 3113–3127. https://doi.org/10.1364/BOE.6.003113.

39. Jiang, Y., Chen, Z., Han, Y., Deb, P., Gao, H., Xie, S., Purohit, P., Tate, M.W., Park, J., Gruner, S.M., et al. (2018). Electron ptychography of 2D materials to deep sub-angstrom resolution. Nature *559*, 343–349. https://doi.org/10.1038/s41586-018-0298-5.

40. Ji, N., Milkie, D.E., and Betzig, E. (2010). Adaptive optics via pupil segmentation for high-resolution imaging in biological tissues. Nat. Methods *7*, 141–147. https://doi.org/10.1038/nmeth.1411.

41. Wu, J., Guo, Y., Deng, C., Zhang, A., Qiao, H., Lu, Z., Xie, J., Fang, L., and Dai, Q. (2022). An integrated imaging sensor for aberration-corrected 3D photography. Nature *612*, 62–71. https://doi.org/10.1038/s41586-022-05306-8.

42. d'Arcy, J.A., Collins, D.J., Rowland, I.J., Padhani, A.R., and Leach, M.O. (2002). Applications of sliding window reconstruction with Cartesian sampling for dynamic contrast enhanced MRI. NMR Biomed. *15*, 174–183. https://doi.org/10.1002/nbm.755.

43. Ma, Y., Li, D., Smith, Z.J., Li, D., and Chu, K. (2018). Structured illumination microscopy with interleaved reconstruction (SIMILR). J. Biophotonics *11*, e201700090. https://doi.org/10.1002/jbio.201700090.

44. Huang, X., Fan, J., Li, L., Liu, H., Wu, R., Wu, Y., Wei, L., Mao, H., Lal, A., Xi, P., et al. (2018). Fast, long-term, super-resolution imaging with Hessian structured illumination microscopy. Nat. Biotechnol. *36*, 451–459. https://doi.org/10.1038/nbt.4115.

45. Descloux, A., Grußmayer, K.S., and Radenovic, A. (2019). Parameter-free image resolution estimation based on decorrelation analysis. Nat. Methods *16*, 918–924. https://doi.org/10.1038/s41592-019-0515-7.

46. Zhang, Y., Lu, Z., Wu, J., Lin, X., Jiang, D., Cai, Y., Xie, J., Wang, Y., Zhu, T., Ji, X., and Dai, Q. (2021). Computational optical sectioning with an incoherent multiscale scattering model for light-field microscopy. Nat. Commun. *12*, 6391. https://doi.org/10.1038/s41467-021-26730-w.

47. Podgorski, K., and Ranganathan, G. (2016). Brain heating induced by near-infrared lasers during multiphoton microscopy. J. Neurophysiol. *116*, 1012–1023. https://doi.org/10.1152/jn.00275.2016.

48. Yildirim, M., Sugihara, H., So, P.T.C., and Sur, M. (2019). Functional imaging of visual cortical layers and subplate in awake mice with optimized three-photon microscopy. Nat. Commun. *10*, 177. https://doi.org/10.1038/s41467-018-08179-6.

49. Maas, A.I.R., Stocchetti, N., and Bullock, R. (2008). Moderate and severe traumatic brain injury in adults. Lancet Neurol. *7*, 728–741. https://doi.org/10.1016/S1474-4422(08)70164-9.

50. Jassam, Y.N., Izzy, S., Whalen, M., McGavern, D.B., and El Khoury, J. (2017). Neuroimmunology of traumatic brain injury: time for a paradigm shift. Neuron *95*, 1246–1265. https://doi.org/10.1016/j.neuron.2017.07.010.

51. Flierl, M.A., Stahel, P.F., Beauchamp, K.M., Morgan, S.J., Smith, W.R., and Shohami, E. (2009). Mouse closed head injury model induced by a weight-drop device. Nat. Protoc. *4*, 1328–1337. https://doi.org/10.1038/nprot.2009.148.

52. Grutzendler, J., Kasthuri, N., and Gan, W.B. (2002). Long-term dendritic spine stability in the adult cortex. Nature *420*, 812–816. https://doi.org/10.1038/nature01276.

53. Rustenhoven, J., Drieu, A., Mamuladze, T., de Lima, K.A., Dykstra, T., Wall, M., Papadopoulos, Z., Kanamori, M., Salvador, A.F., Baker, W., et al. (2021). Functional characterization of the dural sinuses as a neuroimmune interface. Cell *184*, 1000–1016.e27. https://doi.org/10.1016/j.cell.2020.12.040.

54. Verweij, F.J., Balaj, L., Boulanger, C.M., Carter, D.R.F., Compeer, E.B., D'Angelo, G., El Andaloussi, S., Goetz, J.G., Gross, J.C., Hyenne, V., et al. (2021). The power of imaging to understand extracellular vesicle biology in vivo. Nat. Methods *18*, 1013–1026. https://doi.org/10.1038/s41592-021-01206-3.

55. Yu, S., and Yu, L. (2022). Migrasome biogenesis and functions. FEBS Journal *289*, 7246–7254. https://doi.org/10.1111/febs.16183.

56. Ma, L., Li, Y., Peng, J., Wu, D., Zhao, X., Cui, Y., Chen, L., Yan, X., Du, Y., and Yu, L. (2015). Discovery of the migrasome, an organelle mediating release of cytoplasmic contents during cell migration. Cell Res. *25*, 24–38. https://doi.org/10.1038/cr.2014.135.

57. Jiang, D., Jiang, Z., Lu, D., Wang, X., Liang, H., Zhang, J., Meng, Y., Li, Y., Wu, D., Huang, Y., et al. (2019). Migrasomes provide regional cues for organ morphogenesis during zebrafish gastrulation. Nat. Cell Biol. *21*, 966–977. https://doi.org/10.1038/s41556-019-0358-6.

58. Jiao, H., Jiang, D., Hu, X., Du, W., Ji, L., Yang, Y., Li, X., Sho, T., Wang, X., Li, Y., et al. (2021). Mitocytosis, a migrasome-mediated mitochondrial quality-control process. Cell *184*, 2896–2910.e13. https://doi.org/10.1016/j.cell.2021.04.027.

59. Zhang, C., Li, T., Yin, S., Gao, M., He, H., Li, Y., Jiang, D., Shi, M., Wang, J., and Yu, L. (2022). Monocytes deposit migrasomes to promote embryonic angiogenesis. Nat. Cell Biol. *24*, 1726–1738. https://doi.org/10.1038/s41556-022-01026-3.

60. Victora, G.D., and Nussenzweig, M.C. (2012). Germinal centers. Annu. Rev. Immunol. *30*, 429–457. https://doi.org/10.1146/annurev-immunol-020711-075032.

61. De Silva, N.S., and Klein, U. (2015). Dynamics of B cells in germinal centres. Nat. Rev. Immunol. *15*, 137–148. https://doi.org/10.1038/nri3804.

62. Liu, D., Xu, H., Shih, C., Wan, Z., Ma, X., Ma, W., Luo, D., and Qi, H. (2015). T-B-cell entanglement and ICOSL-driven feed-forward regulation of germinal centre reaction. Nature *517*, 214–218. https://doi.org/10.1038/nature13803.

63. Pierangeli, D., Tavani, A., Di Mei, F., Agranat, A.J., Conti, C., and DelRe, E. (2017). Observation of replica symmetry breaking in disordered nonlinear wave propagation. Nat. Commun. *8*, 1501. https://doi.org/10.1038/s41467-017-01612-2.

64. Kasai, H., Fukuda, M., Watanabe, S., Hayashi-Takagi, A., and Noguchi, J. (2010). Structural dynamics of dendritic spines in memory and cognition. Trends Neurosci. *33*, 121–129. https://doi.org/10.1016/j.tins.2010.01.001.

65. Luo, L. (2021). Architectures of neuronal circuits. Science *373*, eabg7285. https://doi.org/10.1126/science.abg7285.

66. Li, X., Li, Y., Zhou, Y., Wu, J., Zhao, Z., Fan, J., Deng, F., Wu, Z., Xiao, G., He, J., et al. (2023). Real-time denoising enables high-sensitivity fluorescence time-lapse imaging beyond the shot-noise limit. Nat. Biotechnol. *41*, 282–292. https://doi.org/10.1038/s41587-022-01450-8.

67. Li, X., Zhang, G., Wu, J., Zhang, Y., Zhao, Z., Lin, X., Qiao, H., Xie, H., Wang, H., Fang, L., and Dai, Q. (2021). Reinforcing neuron extraction and spike inference in calcium imaging using deep self-supervised denoising. Nat. Methods *18*, 1395–1400. https://doi.org/10.1038/s41592-021-01225-0.

68. Bao, F., Deng, Y., Wan, S., Shen, S.Q., Wang, B., Dai, Q., Altschuler, S.J., and Wu, L.F. (2022). Integrative spatial analysis of cell morphologies and transcriptional states with MUSE. Nat. Biotechnol. *40*, 1200–1209. https://doi.org/10.1038/s41587-022-01251-z.

69. Li, T., Fu, T.M., Wong, K.K.L., Li, H., Xie, Q., Luginbuhl, D.J., Wagner, M.J., Betzig, E., and Luo, L. (2021). Cellular bases of olfactory circuit assembly revealed by systematic time-lapse imaging. Cell *184*, 5107–5121.e14. https://doi.org/10.1016/j.cell.2021.08.030.

70. Masuda, T., Amann, L., Monaco, G., Sankowski, R., Staszewski, O., Krueger, M., Del Gaudio, F., He, L., Paterson, N., Nent, E., et al. (2022). Specification of CNS macrophage subsets occurs postnatally in defined niches. Nature *604*, 740–748. https://doi.org/10.1038/s41586-022-04596-2.

71. Perry, V.H., Nicoll, J.A., and Holmes, C. (2010). Microglia in neurodegenerative disease. Nat. Rev. Neurol. *6*, 193–201. https://doi.org/10.1038/nrneurol.2010.17.

72. Casanova-Acebes, M., Dalla, E., Leader, A.M., LeBerichel, J., Nikolic, J., Morales, B.M., Brown, M., Chang, C., Troncoso, L., Chen, S.T., et al. (2021). Tissue-resident macrophages provide a pro-tumorigenic niche to early NSCLC cells. Nature *595*, 578–584. https://doi.org/10.1038/s41586-021-03651-8.

73. Zhang, Y., Wang, Y., Wang, M., Guo, Y., Li, X., Chen, Y., Lu, Z., Wu, J., Ji, X., and Dai, Q. (2022). Multi-focus light-field microscopy for high-speed large-volume imaging. PhotoniX *3*. https://doi.org/10.1186/s43074-022-00076-y.

74. Wagner, N., Beuttenmueller, F., Norlin, N., Gierten, J., Boffi, J.C., Wittbrodt, J., Weigert, M., Hufnagel, L., Prevedel, R., and Kreshuk, A. (2021). Deep learning-enhanced light-field imaging with continuous validation. Nat. Methods *18*, 557–563. https://doi.org/10.1038/s41592-021-01136-0.

75. Wang, Z., Zhu, L., Zhang, H., Li, G., Yi, C., Li, Y., Yang, Y., Ding, Y., Zhen, M., Gao, S., et al. (2021). Real-time volumetric reconstruction of biological dynamics with light-field microscopy and deep learning. Nat. Methods *18*, 551–556. https://doi.org/10.1038/s41592-021-01058-x.

76. Qi, H., Cannons, J.L., Klauschen, F., Schwartzberg, P.L., and Germain, R.N. (2008). SAP-controlled T-B cell interactions underlie germinal centre formation. Nature *455*, 764–769. https://doi.org/10.1038/nature07345.

77. Liu, B., and Qi, H. (2022). In vivo migration and Tfh cell interactions. Methods Mol. Biol. *2380*, 99–109. https://doi.org/10.1007/978-1-0716-1736-6_9.

78. Pelli, D.G. (1997). The VideoToolbox software for visual psychophysics: transforming numbers into movies. Spat. Vision *10*, 437–442.

79. Boyd, S. (2010). Distributed optimization and statistical learning via the alternating direction method of multipliers. FNT in Machine Learning *3*, 1–122. https://doi.org/10.1561/2200000016.

80. Song, A., Gauthier, J.L., Pillow, J.W., Tank, D.W., and Charles, A.S. (2021). Neural anatomy and optical microscopy (NAOMi) simulation for evaluating calcium imaging methods. J. Neurosci. Methods *358*, 109173. https://doi.org/10.1016/j.jneumeth.2021.109173.

81. Pnevmatikakis, E.A., and Giovannucci, A. (2017). NoRMCorre: an online algorithm for piecewise rigid motion correction of calcium imaging data. J. Neurosci. Methods *291*, 83–94. https://doi.org/10.1016/j.jneumeth.2017.07.031.

82. Pnevmatikakis, E.A., Soudry, D., Gao, Y., Machado, T.A., Merel, J., Pfau, D., Reardon, T., Mu, Y., Lacefield, C., Yang, W., et al. (2016). Simultaneous denoising, deconvolution, and demixing of calcium imaging data. Neuron *89*, 285–299. https://doi.org/10.1016/j.neuron.2015.11.037.

83. Deitch, D., Rubin, A., and Ziv, Y. (2021). Representational drift in the mouse visual cortex. Curr. Biol. *31*, 4327–4339.e6. https://doi.org/10.1016/j.cub.2021.07.062.

Please cite this article in press as: Zhao et al., Two-photon synthetic aperture microscopy for minimally invasive fast 3D imaging of native subcellular behaviors in deep tissue, Cell (2023), https://doi.org/10.1016/j.cell.2023.04.016

STAR★METHODS

KEY RESOURCES TABLE

REAGENT or RESOURCE	SOURCE	IDENTIFIER
Antibodies		
Anti-Ly-6G/Ly-6C (RB6-8C5), PE	eBioscience	12-5931-82; RRID: AB_466045
Alexa Fluor CD11b	Biolegend	Cat# 101217; RRID: AB_389305
PE anti-CD86	Biolegend	Cat# 105007; RRID: AB_313150
BB700 anti-CD19	BD Biosciences	Cat# 566411; RRID: AB_2744315
Bacterial and virus strains		
AAV2/2Retro-Plus-hSyn-Cre-WPRE-pA	Taitool Bioscience	Cat# S0278-2RP-H20
AAV2/9-hSyn-DIO-jGCaMP7b-WPRE-pA	Taitool Bioscience	Cat# S0592-9-H50
Chemicals, peptides, and recombinant proteins		
Propidium iodide (PI)	RuiTaibio	P2012-4
DAPI	Solarbio	C0060-1ml
FluoSpheres™ Carboxylate-Modified Microspheres, 0.2 μm	ThermoFisher	F8811
1μg per ml lipopolysaccharide (LPS)	Sigma	L6143-1mg
Critical commercial assays		
USAF-1951 resolution chart	Ready Optics	2015a Extreme USAF
Mouse B cells positive isolation kit	Miltenyi Biotec	130-121-301
Mouse B cells CD43 MicroBeads	Miltenyi Biotec	130-097-148
Mouse T cells CD4 MicroBeadst	Miltenyi Biotec	130-117-043
Glass slide	Citotest	188105
Cover glass	Electron Microscopy Sciences	#72204-01
Experimental models: Organisms/strains		
Drosophila: His2Av-mRFP1 transgenic stocks	Bloomington Stock Center	34498
Thy1-YFP-H transgenic mice	Jackson Stock	003782
CX3CR1-GFP transgenic mice	The Jackson Laboratory	Jax 008451
Mouse: C57BL/J	The Jackson Laboratory	Jax 0664
Mouse: C57BL/J	Charles River Laboratories	N/A
Rasgrf2-2A-dCre;Ai148d mice	The Jackson Laboratory	Jax 022864
Mouse: green fluorescent protein (GFP)-expressing	The Jackson Laboratory	Jax 4353
Mouse: dsRed-expressing	The Jackson Laboratory	Jax 6051
Mouse: OVA323–339-specific T cell-receptor transgenic OT-II	The Jackson Laboratory	Jax 4194
Mouse: HEL-specific Ig-transgenic MD4	The Jackson Laboratory	Jax 2595
Mouse: cyan fluorescent protein (CFP)-expressing	The Jackson Laboratory	Jax 4218
Software and algorithms		
Image J	NIH Image for the Macintosh	https://imagej.nih.gov/ij/index.html
MATLAB	Mathworks	https://www.mathworks.com/products/matlab.html
Amira	ThermoFisher	https://www.thermofisher.com/cn/en/home/industrial/electron-microscopy/electron-microscopy-instruments-workflow-solutions/3d-visualization-analysis-software.html

(*Continued on next page*)

Please cite this article in press as: Zhao et al., Two-photon synthetic aperture microscopy for minimally invasive fast 3D imaging of native subcellular behaviors in deep tissue, Cell (2023), https://doi.org/10.1016/j.cell.2023.04.016

Continued

REAGENT or RESOURCE	SOURCE	IDENTIFIER
Imaris	Oxford Instruments	https://imaris.oxinst.com/
3D reconstruction algorithm with DAO	This paper	https://github.com/BBNCELi/2pSAM_recon
Motion correction with a sliding window algorithm	This paper	https://github.com/BBNCELi/2pSAM_recon
Other		
25×/1.05 NA Water immersion objective	Olympus	XLPLN25XWMP2
Dichroic mirror	Thorlabs	DMSP805L/DMLP490R/DMLP567R/DMLP650R
Emission filter	Chroma	ET610/75m/ET670/50m
Emission filter	Thorlabs	MF460-60/MF525-39
ThermoStar body temperature maintenance instrument	RWD	https://www.rwdls.com/product/operative/case1/804.html

RESOURCE AVAILABILITY

Lead contact

Further information and requests for resources and reagents should be directed to and will be fulfilled by the lead contact, Qionghai Dai (daiqh@tsinghua.edu.cn).

Materials availability

This study did not generate new unique reagents.

Data and code availability

- All data reported in this paper will be shared by the lead contact upon request.
- All original code with example data has been deposited at https://github.com/BBNCELi/2pSAM_recon.
- Any additional information required to reanalyze the data reported in this paper is available from the lead contact upon request.

EXPERIMENTAL MODEL AND SUBJECT DETAILS

Animals

All the experimental procedures were approved by the Use Committee and Institutional Animal Care at Tsinghua University, Beijing, China.

In vitro experiments of cell death and activation

To prepare cells, GFP-expressing B cells were isolated from GFP-expressing B6 mice (Jax 4353, male, 8-12 weeks) using Mouse B cells positive isolation kit (Miltenyi Biotec), according to the manufacturer's protocols. The freshly isolated B cells were suspended in PBS buffer for further use. For the positive control group with activated B cells *in vitro*, B cells were suspended in complete RPMI medium supplemented with 1 μg per ml lipopolysaccharide (LPS; Sigma) and cultured in the 6-well plate for 2 days before being used for imaging.

Drosophila embryos

Drosophila embryo experiments in Video S2 (part III) were performed with His2Av-mRFP1 transgenic stocks (Bloomington stock number 34498). *Drosophila* embryos were dechorionated with 50% (vol/vol) sodium hypochlorite solution (cat. No. 425044, Sigma-Aldrich) and then transferred carefully to the 0.4% agarose (SeaPlaque, Lonza). The temperature of the agarose was elevated to 30°C before the transfer to avoid embryo damage. During 2pSAM imaging, a pump was performed for oxygen supply and embryos were kept at a 25°C standard temperature.

Mouse TBI model

For the TBI model, the closed-head injury was performed by weight drop, as previously described.[51] Briefly, CX3CR1-GFP transgenic mice (Jax 008451, male, 8-12 weeks) were anesthetized using isoflurane (2-3%) to incise the scalp for appropriate exposure of the bony skull. For simultaneous imaging of TBI-induced neutrophil-microglia interactions, 10 μl PE-Ly-6G/Ly-6C (eBioscience, 12-5931-82) dissolved in 200 μl physiological saline were injected into the CX3CR1-GFP transgenic mice by intravenous injection. After that, the anesthetized mice were situated under a device consisting of a metal tube (inner diameter 13 mm) placed vertically

Please cite this article in press as: Zhao et al., Two-photon synthetic aperture microscopy for minimally invasive fast 3D imaging of native subcellular behaviors in deep tissue, Cell (2023), https://doi.org/10.1016/j.cell.2023.04.016

over the animal's head. A sponge immobilization board supported the head to allow some head movements during the injury, analogously to the movements occurring during closed head injury in car accidents. The injury was induced by dropping a 25-gram-weight metal from 80-cm height down through the metal tube, striking the skull. The animals were held in such a way that the impact on the skull was right near the dural sinus.[53] Immediately after the injury, a high-speed drill was carefully used to reduce the skull thickness by about 50%.[52] To avoid damaging the underlying cortex by friction-induced heat, a cool sterile solution was added to the skull periodically, and drilling was intermittent to permit heat dissipation. Skull thinning was completed by scraping the cranial surface with a micro-surgical blade (Surgistar no. 6400). For optimal image quality, skull thickness was reduced to a very thin layer (about 30 μm). Subsequently, mice were implanted with a head bar for 2pSAM imaging. Injured mice were hereon referred to as TBI mice (n = 5). Sham mice (n = 3) underwent the same aforementioned procedure except no injury induction.

Laser-induced injury imaging

For the imaging of laser-induced neutrophil-microglia interactions, 10 μl PE-Ly-6G/Ly-6C (eBioscience, 12-5931-82) dissolved in 200 μl physiological saline were injected into the CX3CR1-GFP transgenic mice (Jax 008451, male, 8-12 weeks) by intravenous injection. A cranial window was completed after injection. Subsequently, mice were implanted with a head bar for 2pSAM imaging. In order to introduce laser-induced injury, the wavelength of the two-photon laser was set at 800 nm with the laser power of about 400 mW at the sample. The beam was parked for approximately 2 s at the desired position to create an injury site. Imaging of the response was started immediately after this laser-induced tissue damage.

Lymph node imaging

For mice, C57BL/6 (Jax 0664), green fluorescent protein (GFP)-expressing (Jax 4353), dsRed-expressing (Jax 6051), OVA323–339-specific T cell-receptor transgenic OT-II (Jax 4194) and HEL-specific Ig-transgenic MD4 (Jax 2595) were originally from the Jackson Laboratory. Relevant mice were interbred to obtain dsRed-expressing MD4 and GFP-expressing MD4 mice. Six to twelve-week-old, age- and sex-matched mice were used for the experiments.

For the cell isolation and adoptive transfer, OT-II T and MD4 B cells were isolated from OT-II and MD4 mice, respectively, using the negative CD4 T cell or B cell isolation kit (Miltenyi Biotec). To examine GC formation by MD4 B cells with the help from OT-II T cells, B6 mice received a mixture of freshly isolated cells that consisted of OT-II T cells (4×10^5 per recipient), dsRed-expressing MD4 B cells (3.84×10^5 per recipient) and GFP-expressing MD4 B cells (0.16×10^5 per recipient). B6 recipients were subcutaneously immunized with 130 μg HEL–OVA conjugated antigen emulsified in 50% alum (Thermo Scientific) with 0.5 μg lipopolysaccharide (LPS, Sigma). HEL-OVA conjugated antigens were made by chemical crosslinking with a HydraLink conjugation kit (SoluLink) as previously described.[76]

The surgical procedure for intravital imaging of the inguinal lymph node was then performed as previously described.[76,77] Finally, we put the mouse under the 2pSAM for imaging.

Neural imaging

For neural imaging in Figures 7 and S7, a 3-mm craniotomy was made over the visual cortex (centered at 4.0 mm posterior and 2.5 mm lateral to Bregma) in head-fixed Rasgrf2-2A-dCre;Ai148d mice (Jax 022864, male, 8-12 weeks), leaving the dura intact. A cranial window was implanted over the craniotomy and recovered for at least 2 weeks before imaging.

We used moving grating stimuli generated by the Psychophysics Toolbox[78] on MATLAB R2021a. Within each stimulus trial, we first applied a 4 s moving sinusoidal grating (0.025 cycles per degree, 1 Hz temporal frequency) followed by a 4 s blank period (uniform gray at mean luminance) for each direction. Typically, 4 drifting directions were used (separated by 45 degrees) for each trial. For each round, we conducted 10 trials continuously. In this case, each round lasted for about 320 s and was repeated 5 times with a time interval of 0.25 h. During the interval, we kept imaging to analyze the influence of long-term neural recoding (Figure 7B). The gratings were presented with a 16 × 9 cm^2 LCD monitor, placed 8 cm in front of the center of the left eye of the mouse. During simultaneous imaging, a blue-colored glass filter with a bandwidth of 100 nm and center wavelength of 450 nm was placed in front of the mouse eye to minimize the stimulus contamination for the green detection channel.

For neural imaging in Figure 3D, we injected AAV2/2-Retro-Plus-hSyn-Cre-WPRE-pA (Taitool Bioscience, Cat# S0278-2RP-H20) into the auditory thalamus of C57BL/6J (Wild type) mice (Charles River Laboratories), and injected AAV2/9-hSyn-DIO-jGCaMP7b-WPRE-pA (Taitool Bioscience, Cat# S0592-9-H50) into the auditory cortex. Three weeks after the injections, the cranial window was opened upon the mouse's head. After the removal of parts of the temporalis muscles, a 3-mm-diameter cranial window whose center was located at 3 mm posterior to the Bregma was opened on the temporal cortical surface and a 3-mm-diameter circular coverslip (170 μm thick) was implanted onto the exposed surface and sealed by the tissue glue and dental cement. Then we imaged the pyramidal neurons at different cortical layers by different configurations to compare the penetration depth of 2pSAM and TPM.

Evaluation of 2pSAM on different wavelengths

The samples were prepared as below (Figure 2E). To image CFP fluorophores, cyan fluorescent protein-expressing mice (Jax 4218, male, 8-12 weeks) were bred with MD4 mice to obtain MD4-CFP mice. As mentioned before, MD4-CFP B cells (1×10^5 per recipient) and OT-II T cells (2×10^5 per recipient) were isolated and co-transferred into B6 mice. These B6 mice were subcutaneously immunized with HEL-OVA. Then the lymph node was performed to be imaged in TPM and 2pSAM system. To image far-red dyes, freshly

isolated mouse B cells were incubated with BB700 anti-CD19 (1D3, BD Biosciences) at the concentration of 1:200 for 30 minutes on ice and then washed with PBS buffer. Then BB700-labeled B cells were dropped on the glass slide and imaged in TPM and 2pSAM systems. To observe the signals of second harmonic generation (SHG), mouse lymph node was exposed following the above protocols and performed in TPM and 2pSAM system. For imaging of DAPI dye, 10 μl of DAPI (C0060-1ml, Solarbio) stock solution was injected into the cortical layer 2/3 of C57BL6/J mice (Jax 0664, male, 8-12 weeks) through glass electrodes. A thin skull imaging window was opened near the injection site for both TPM and 2pSAM imaging under the same laser power.

Slice preparation

For the preparation of Thy1-YFP mouse brain slices, Thy1-YFP-H transgenic mice (Jackson stock No. 003782, age > P60, male) were used. Mice were perfused transcardially with 50 mL of 0.01 M PBS followed by 25 mL of 4% PFA (dissolved in 0.01 M PBS). The brain was harvested and postfixed in 4% PFA overnight at 4 °C. Both 50-μm-thick and 100-μm-thick slices were cut using a vibratome (VT1200 S, Leica) at room temperature. The slices were then sealed in antifade solution (C1210, Applygen Technologies, Inc.) for long-term storage at 4 °C. Finally, the slices were mounted directly for imaging.

METHOD DETAILS

Experimental setup

The system diagram is shown in Figure S1A. The 2pSAM system can be used as a compact add-on for any existing two-photon imaging system by inserting the PSF modulation part at the beginning of the excitation path. In practice, we built up a system to integrate three different configurations together for the convenience of comparison, including traditional TPM mode, mid-NA 2pSAM mode, and min-NA 2pSAM mode. We used the commercial femtosecond laser (Spectra-Physics InSight X3, Newport) for two-photon excitation with a pulse duration of about 120 fs and a repetition rate of 80 MHz. The central wavelength for most experiments was 920 nm unless otherwise stated. An electro-optic modulator (350-80LA-02, Conoptics) with a half wave plate was used to adjust the excitation power at extreme speed. Then we used multiple electrical flip mirrors (FM) to switch among three different configurations in the excitation path. For TPM mode, the laser beam was directly expanded by a 4*f* system with a magnification factor of 3 to entirely fill the back pupil plane of the objective (25×/1.05 NA, water-immersion, Olympus, XLPLN25XWMP2) for high-NA excitation. For the 2pSAM modes, we generated the needle-like beams by using two 4*f* systems to reduce the relative beam size at the pupil plane about α times pupil size, where the ratio α corresponded to the ratio between the small sub-aperture NA and the whole-objective NA. We used two different lenses (L3 with a focal length of 500 mm and L3' with a focal length of 250 mm) to modify the magnification factor of the 4*f* system, equivalently adjusting the ratio α, which could balance the snapshot volumetric imaging range and the spatial resolution. For mid-NA 2pSAM, we set the ratio α as 0.1 to achieve near-diffraction-limited resolution near the focal plane with an effective volumetric imaging range of about 25 μm. For min-NA 2pSAM, we set the ratio α as 0.05 to achieve sub-micron resolution near the focal plane with an effective volumetric imaging range of about 100 μm. A 100-μm pinhole was placed at the focal plane of the first 4*f* system to introduce the ptychographic constraint for the phase correlation between different angular beams, which is critical for synthetic aperture up to the diffraction limit of the whole objective NA, indicated by the comparisons of the OTFs in Figures 1C and 1E. The size of the pinhole is close to the Abbe diffraction limit of the sub-aperture excitation beam, corresponding to about 3.92 μm for mid-NA and 7.85 μm for min-NA at the objective plane for the experimental system. Large pinhole size will reduce the effect of ptychographic constraint, leading to reduced synthesized resolution, while narrow pinhole size results in the loss of DOF and laser power (Figure S2). Then we placed a tip/tilt piezo mirror (S-335, PI) at the focal plane of the second 4*f* system to change the angles of the needle-like beam at high speed up to 200 Hz. By changing the angles at the conjugated objective plane, we can scan the whole back pupil of the objective lens. We used 13 different angles in all of our experiments, since the reconstruction performance converges with the increase of the angle number in current configurations (Figure S2). After the PSF modulation part, the 2pSAM mode shares the same optical path as the TPM mode for both two-dimensional spatial scanning and multi-color epi-fluorescence collection. We used a resonant mirror (CRS8KHz, Cambridge Technology) and a galvanometer (8315K, Cambridge Technology) for high-speed scanning with a scan lens (SL50-2P2, Thorlabs) and a tube lens (TL200-2P2, Thorlabs) to relay the beam to the objective for two-photon excitation. The focal lengths of all the lenses are listed as below: 200 mm (L1, TL), 100 mm (L2, L7), 500mm (L3), 250 mm (L3'), 109 mm (L4), 80 mm (L5, L6), 300 mm (L8), 50 mm (L9, L10, L11, L12, SL). For multi-color fluorescence collection simultaneously, we used the combination of four dichromatic mirrors (DMSP805L, DMLP490R, DMLP567R, DMLP650R, Thorlabs), four filters (MF460-60, MF525-39, Thorlabs; ET610/75m, ET670/50m, Chroma), and 4 PMTs (H10770PA-40, Hamamatsu). For the observation of *Drosophila* embryo development, we adjusted the excitation wavelength to 1100 nm for better excitation efficiency. Mechanical axial scanning was performed by the sample stage (M-VP-25XA-XYZL, Newport) and the piezo objective scanner (P725, PI). The detailed imaging and reconstruction parameters for all the experiments were provided in Table S1. All the laser powers indicated in our work are measured at the output of the objective, corresponding to the powers at the sample.

3D reconstruction algorithm with DAO

Instead of point scanning in 3D space for traditional TPM, 2pSAM uses correlated needle-like beams to capture projections of the entire volume along different angles, akin to the tomographic process in light-field microscopy[5] (Figure 1A). Therefore, a 3D deconvolution algorithm was used to reconstruct the depth-resolved 3D information. In the meantime, as different angular projections

correspond to different sub-apertures of whole-objective NA, the aberrated wavefront leads to different lateral shifts of these angular measurements (Figure 1G). The disparities between these angular measurements are proportional to the wavefront gradients of corresponding sub-aperture, which could be used to estimate the optical aberrations introduced by imperfect imaging systems or nonuniform refractive index distributions in tissue, without the requirement of additional wavefront sensors or iterative feedback in traditional AO techniques (Figures S2J and S2K). We have also shown that the needle-like beams of 2pSAM themselves are considerably more robust than high-NA excitation in TPM under the same optical aberrations, leading to better SNR and resolution in raw measurements (Figures 1H, 1I, and 2F). Moreover, these aberrations could then be used to generate aberrated PSFs during 3D deconvolution to correct the aberrations in post-processing. This process including both aberration estimation and correction is termed as DAO, which has already been verified in one-photon light-field microscopy[5] but has never been exploited in two-photon imaging. In this case, multi-site aberration correction for spatially nonuniform aberrations can be conducted simultaneously by dividing the FOV during reconstruction without reducing the imaging speed (Video S1, part II).

In practice, we used an alternating direction method of multipliers (ADMM) algorithm[79] to update the aberration-corrected 3D volume and the aberration wavefront iteratively. The optimization problem can be described as below:

$$g(x,z), S(x,u) = \underset{g(x,z),S(x,u)}{\operatorname{argmax}} \Pr_{\text{Pois}}\left(M(x,u)\middle|\int g(x,z) * H(x + S(x,u),z,u)dz\right),$$

$$\text{s.t. } g(x,z) \geq 0,$$

where $g(x,z)$ is the volume to be reconstructed; x,z,u correspond to the lateral coordinate, axial coordinate, and the angular coordinate; $S(x,u)$ is the disparity map resulting from the optical aberrations and motion, from which the aberration phase can be recovered through a phase retrieval algorithm; $M(x,u)$ is the raw angular measurement captured by 2pSAM for the angle u; $\Pr_{\text{Pois}}$ is the probability function of Poisson distribution, i.e. $\Pr_{\text{Pois}}(X|\lambda) = \frac{\lambda^X e^{-\lambda}}{X!}$; $H(x,z,u)$ represent the PSF; $*$ is the convolution operator.

The flowchart of the whole pipeline is shown in Figure S1B. Within each iteration k, we first conducted phase-space deconvolution for each angle u sequentially to update the volume $g_u^k(x,z)$ with the measurements $M(x,u)$ and simulated angular PSFs $H(x,z,u)$.[5] The shift vector $S(u)$ corresponded to the lateral shifts of the angular PSFs induced by the aberration, which was estimated in previous iteration and set as zeros for the first iteration. After going through all the angles (13 angles for all the experiments here), we estimated the aberration gradient, or shift vector $S(u)$, by calculating the disparities between the forward projections and the angular measurements as $\text{Disp}(P(x,u),M(x,u))$. Specifically, we calculated the correlation map between the forward projection and measurement for each angle and found the zero offsets of the maxima. Then the current shift vector was used for the next volume update. Finally, we obtained both the aberration-corrected volume and the aberration wavefront estimated from the integral of the phase gradient map $S(u)$. The estimated aberration wavefront can also be used during the PSF generation process to obtain a more accurate description of the imaging model, especially for the system aberration, which can be calibrated in advance. For multi-site aberration correction, we divide the large FOV into multiple small tiles with the overlap between each tile. Once we obtained the shift maps for each tile, we used linear interpolation to estimate the shifts in the overlapped region for smooth transition between different tiles based on the assumption that the aberrations change smoothly within the whole FOV. Since the reconstruction performance for either sparse or dense samples converges quickly with the increase of iteration number in different SNR conditions, we normally choose the iteration number of 10 for all the samples (Figures S1D and S1E). It generally takes about 13 seconds for 10 iterations of a volume covering 512×512×101 voxels on a desktop computer (CPU: Intel i9-10900X, RAM: 128 GB, GPU: NVIDIA GeForce RTX 3090) by our proof-of-concept implementations based on MATLAB R2021a. For the reconstruction of a single volume, we used the all-ones matrix as the initial volume. For continuous video reconstruction, we used the reconstructed volume of the former frame as the initial volume of the current frame to accelerate the reconstruction process with only 2 iterations for each volume. Moreover, learning-based reconstructions can be exploited in the future to further accelerate the reconstruction process.

We chose simulated PSFs instead of experimental PSFs for reconstruction, as the latter could be easily disturbed by noise or stage instability. To generate the PSFs as accurately as possible, we first conducted a system calibration to estimate the imaging parameters, including the ratio α, the pinhole diameter as well as the tilting angles of the needle-like beams (see system calibration). Then we can obtain the representation of the PSFs by describing the light propagation process in wave optics model from the laser output to the objective plane, including the pinhole, angle-scanning by the tip/tilt piezo mirror, and the magnification of the excitation system. Therefore, the PSF for a specific angle can be represented as below:

$$H(x,z,u) = \left\| \mathcal{F}^{-1}\left\{ \mathcal{F}\left[\mathcal{F}^{-1}(Pupil_{sub}(f_x)\cdot\mathcal{F}(U(x)))\cdot Pinhole(x)\cdot e^{ik_u x}\right]\cdot Pupil_{obj}(f_x)\cdot e^{i\phi(f_x)}\cdot e^{i2\pi\frac{z}{\lambda}\sqrt{1-(\lambda f_x)^2}}\right\}\right\|_2^4,$$

where $\mathcal{F}(\cdot)$ and $\mathcal{F}^{-1}(\cdot)$ represent 2D Fourier transform and inverse Fourier transform. x and z are the lateral and axial coordinates, respectively. f_x is the lateral coordinate in the back pupil plane. $U(x)$ is the complex field of a point source. λ means the wavelength of excitation laser. $Pupil_{sub}(f_x)$ and $Pupil_{obj}(f_x)$ correspond to the pupil function of the sub-aperture component and the objective lens,

working as the low-pass circular filters. For 2pSAM (mid, 1.05 NA) system, $Pupil_{sub}(f_x)$ corresponds to the pupil function of 0.105 NA circular intensity modulation, and $Pupil_{obj}(f_x)$ corresponds to the pupil function of 1.05NA circular intensity modulation. $Pinhole(x)$ is the intensity modulation of the ptychographic pinhole, whose size is close to the Abbe diffraction limit of the sub-aperture NA. k_u represents the position of the sub-aperture at the back pupil plane, corresponding to the tilting angle of the tip/tilt piezo mirror. $\phi(f_x)$ is the aberration phase, which can be calibrated in advance or estimated by the DAO algorithm (Figure S1). The item $e^{i2\pi\frac{z}{\lambda}\sqrt{1-(\lambda f_x)^2}}$ is the defocus term.

System calibration

The experimental system may have deviations with the schematic design. As a computational imaging method using the simulated PSF for reconstruction, 2pSAM requires system calibration to estimate the key parameters for accurate PSF generation. We estimated these parameters by imaging the 200-nm-diameter fluorescence bead. For the ratio α between the sub-aperture NA and the whole-objective NA, we adjusted the input laser beam size to match the experimental dof without pinhole the same as the theoretical DOF of the sub-aperture NA without the pinhole. For the relative diameter of the pinhole at the objective plane, depending on the actual magnification factor of the system, we used the FWHM of the bead located at the focal plane during 2pSAM imaging of the center angle. For the tilting angles of the angular PSFs, we estimated from the angles of the experimental PSF, corresponding to the relative shifts of the sub-apertures at the back pupil plane controlled by the tip/tilt piezo mirror. For the optical aberrations of the imaging system itself, we used our DAO algorithm to estimate the aberrations by imaging the fluorescence beads. And the system aberration was used as the initial aberration during reconstruction in all the experiments. All of these calibrations were conducted only once after the system was set up.

Motion correction with a sliding window

2pSAM requires multiple angular projections (13 here) to reconstruct the volume. Although we used a sliding window to maintain the temporal sampling density as rapidly as 2D scanning, the sample dynamics of either morphological changes or intensity fluctuations may result in reconstruction artefacts (Figure S3). We then conducted a series of numerical simulations to quantitatively analyze the motion influence and verify the effectiveness of the sliding window.

There is spatiotemporal continuity for time-lapse imaging of most fluorescence samples, otherwise it means that the phenomenon is greatly faster than the sampling speed. To analyze the influence on morphological dynamics, we simulated the sample moving at different speeds during imaging. For samples with sharp edges, we simulated a resolution chart at the focal plane. For samples with blurry structures, we simulated 3D neurons distributed in cortex using *in silico* neural anatomy and optical microscopy (NAOMi) simulation.[80] We developed a motion correction algorithm by merely conducting only 1 iteration of reconstruction to estimate the shift vectors as the motion-induced disparities. Then we used these motion-induced shift vector to shift the measurements in preprocessing for motion registration and reconstruct the volume again. Image blur caused by sample motion can be restored to high spatial resolution through motion correction (Figure S3B). Meantime, the sliding window can additionally restore the time resolution during sample movement (Figure S3A). Furthermore, we found that DAO itself showed great robustness to sample motions (Figure S3B). Because movement-induced lateral shifts hold the same characters as the aberration-induced ones, which can also be corrected during iterative reconstruction. However, for particularly large movements in samples with smooth structures, the initial reconstructed volume is distorted too much to be corrected. More iterations can be used to improve the robustness of the motion correction algorithm (Figure S3E). As shown in Figures S3B–S3E, the motion correction algorithm could preserve the resolution well and eliminate the motion artefacts even for extremely large motions up to 180 pixels during angular scanning for the images with only 512×512 pixels.

For intensity fluctuations such as calcium imaging, we simulated large-scale time-series calcium data sets using NAOMi.[80] Then we simulated the imaging process of the 2pSAM by convolution of the ground-truth volumes with corresponding angular PSFs in order. The reconstruction results with the sliding window show better temporal resolution and has considerably higher Pearson correlation with the ground truth calcium traces, indicating the effectiveness of the sliding window to preserve the temporal resolution (Figures S3F–S3H).

Numerical simulation

For all the numerical simulations to evaluate the performance of 2pSAM, we simulated the captured images by convolution of the ground truth images with the simulated PSFs at the center wavelength of 920 nm. All the simulations were conducted with MATLAB R2021a on a desktop computer (CPU: Intel i9-10900X, RAM: 128 GB, GPU: NVIDIA GeForce RTX 3090). We used the same PSF model as described in the reconstruction algorithm and adjusted corresponding parameters, including the pinhole size, the NA ratio α, angle number (Figure S2) to evaluate their influence on DOF, resolution, and energy distributions. We chose the parameters for mid-NA and min-NA configurations based on the numerical simulations and found the experimental results fit nicely with the simulation after system calibration. For the ground truth data of the numerical simulation, we used NAOMi to generate the neural distributions in scattering tissue,[80] setting the imaging depth to 200 μm beneath the mouse skull. In addition, to further analyze the influence of the sample density on reconstruction performance, we generated the data in NAOMi with different labeling densities of neurons. We used the structural similarity index measure (SSIM) as the main evaluation metric. We added different levels

Please cite this article in press as: Zhao et al., Two-photon synthetic aperture microscopy for minimally invasive fast 3D imaging of native subcellular behaviors in deep tissue, Cell (2023), https://doi.org/10.1016/j.cell.2023.04.016

of Gaussian noises to generate different SNR conditions for convenience. As shown in Figures S1D and S1E, 2pSAM shows similar performance for different sample densities under different SNR conditions. All of the numerical simulation experiments were indicated and specified in the figure legends.

Mouse experiments

All the experimental procedures were approved by the Use Committee and Institutional Animal Care at Tsinghua University, Beijing, China.

Immune cell imaging in cortex

For imaging of immune cells, 10 μl PE-Ly-6G/Ly-6C (eBioscience, 12-5931-82) and 10 μl Alexa Fluor CD11b (Biolegend, 101217) dissolved in 200 μl physiological saline were injected into C57BL6/J mice (Jax 0664, male, 8-12 weeks) by intravenous injections. A cranial window was completed after injection. Subsequently, mice were implanted with a head bar for 2pSAM imaging in the cortex. For endoscopic deep tissue imaging, all the above procedures were the same except that a GRIN lens (NEM-050-06-08-520-S-0.5p, GRINTECH GmbH) was implanted into the cranial window before imaging. The same laser power was used during comparisons between TPM and 2pSAM.

Detection of dead or activated cells

For imaging of dead cells *in vivo* in Figure 4, 10 μl of propidium iodide (PI, RuiTaibio) at a concentration of 1% of the original fluid was injected into the cortical layer 2/3 of C57BL6/J mice (Jax 0664, male, 8-12 weeks) through glass electrodes. A thin skull imaging window was opened near the injection site for both TPM and 2pSAM imaging under the same laser power.

For *in vitro* imaging in Figures 4 and S4, cell death is indicated by propidium iodide (PI) staining (P2012-4, RuiTaibio) and B cell activation is indicated by CD86 (GL-1. PE anti-CD86, Biolegend). The mixture of the indicated staining dye or antibody with one drop of single cell suspension that appropriately contains 105 cells was dropped in the middle of glass slide (188105, Citotest) and then covered by the cover glass (#72204-01, Electron Microscopy Sciences). Then we conducted *in vitro* imaging by both TPM and 2pSAM for comparisons. For the *in vitro* cell death experiment, both TPM and 2pSAM were used to image the samples continuously for an hour at similar 3D imaging speed (25 planes at the interval of 1 μm for TPM; 13 angles for mid-NA 2pSAM) under the same excitation power of 50 mW (Figure S4B). For the control experiment, we only imaged the sample through TPM by two times, corresponding to the time point of 0 min and 60 min (Figure S4C). We repeated the experiments by 6 times for statistical analysis. For the *in vitro* activation experiment, we set up three groups of cells that were TPM-exposed, 2pSAM-exposed and, not-exposed, respectively, with similar cellularity. For the TPM-exposed group, we continuously imaged the sample of freshly isolated B cells with anti-CD86 antibody for 1 hour to activate B cells (Figure S4D). 6 hours later, we recorded the sample in the same region. For the 2pSAM-exposed group, we continuously imaged the sample for 7 hours to activate B cells (Figure S4E). For the negative control group, we only recorded the sample twice at the start and end time points in the same region (Figure S4F). For the positive control group, we also imaged the sample of the activated B cells with anti-CD86 antibody (Figure S4G).

QUANTIFICATION AND STATISTICAL ANALYSIS

Image analysis

All the data analyses were done with customized Matlab R2021a (Mathworks) programs and Imaris 9.3 (Oxford Instruments).

Calcium imaging analysis

The calcium imaging data were processed on Matlab R2021a (Mathworks). First, we performed motion correction using a piecewise rigid motion correction algorithm.[81] Next, we used CNMF[82] directly for cell segmentation and trace extraction. To analyze neural responses to visual stimulus, we selected out the visual-stimulus-related neurons based on a collective measure of the reliability of the neurons using time-shuffled data. Specifically, a neuron's activity on each trial in the first round was circularly shuffled by a random amount and repeated 5000 times. The most correlated 10 or 20 neurons were selected out for visualization and analyzing. For the t-distributed stochastic neighbor embedding (tSNE) analysis (Figure 7D), we used the temporal traces during the visual stimulus of a specific direction in each trial as the input vector. We used a total of 600 time-windows as the input vector for tSNE analysis. To obtain the correlation map among different rounds (Figure 7E), we calculated the Pearson's correlation coefficients between the trial-averaged post-stimuli response of each individual neuron and used the mean value across all the 10 neurons selected to capture the central tendency of the entire population, as described in Deitch et al.[83] When comparing the strength of neural activities in Figure 7G, we calculated the standard deviation of the temporal traces of the visual-stimulus-related neurons during 10-trial visual stimulus within one round, and box-plotted the results of these 20 neurons for both 2pSAM (mid) and TPM. To compare the changes of the neural-activity strength, we normalized the curves by their mean value in the first rounds. For k-means clustering in Figure 7H, we split out the temporal traces into four stages (during-stimulus, between-stimulus gray screen, between-round gray screen, and the whole gray screen), and used their standard deviations during corresponding stages as features for each neuron, representing their activities during this period. We then used k-means method to separate neurons into four clusters based on these features. For

Please cite this article in press as: Zhao et al., Two-photon synthetic aperture microscopy for minimally invasive fast 3D imaging of native subcellular behaviors in deep tissue, Cell (2023), https://doi.org/10.1016/j.cell.2023.04.016

2D visualization, we used the principal component analysis (PCA) method to reduce the feature dimensionality from 4 to 2, after which the groups of neurons can be precisely distinguished as in Figure 7H.

Cell tracking

We used the commercial software Imaris 9.3 to track the cell movements. For GC cell tracking in Figures 6 and S6, we regarded B cells as spots with a diameter of 10 μm. We filtered the trajectories to ensure that a spot was tracked for at least 10 minutes. For microglia tracking in Figures S5F–S5I, we created surfaces to estimate the contours of cells. The linkage of these contours increased the tracking accuracy as they took the morphological changes of cells into consideration.

SBR calculation

For the calculation of SBR in Figure 4, we first normalized the whole image either for raw data or reconstructed slice. Then a line across a typical structure (including the background around the structure) was drawn, and the intensity distribution along the line was obtained. We used the maximum value of the line as the signal S, and averaged the intensity value within the range of 3 μm at the beginning and the end of the line as the background B. Finally, SBR can be obtained by SBR = (S-B)/B.

Cell death

For the definition of dead cells with PI labeling, cells with a large fluorescence intensity in the channel of PI were regarded as dead cell. For the definition of dead cells in CX3CR1-GFP mice, the cells with ablation of soma were regarded as dead cells. The mortality rate corresponds to the ratio between the number of dead cells during the imaging duration and the number of live cells at 0 min. The dead cells at 0 min were not counted.

Statistical analysis

All the statistical tests were performed by Matlab R2021a (Mathworks). Normally distributed data were presented as mean values together with the standard deviation. All of the statistical details of experiments, specifically the size and type of individual samples, n, were indicated and specified in the figure legends.

CellPress
OPEN ACCESS

Supplemental figures

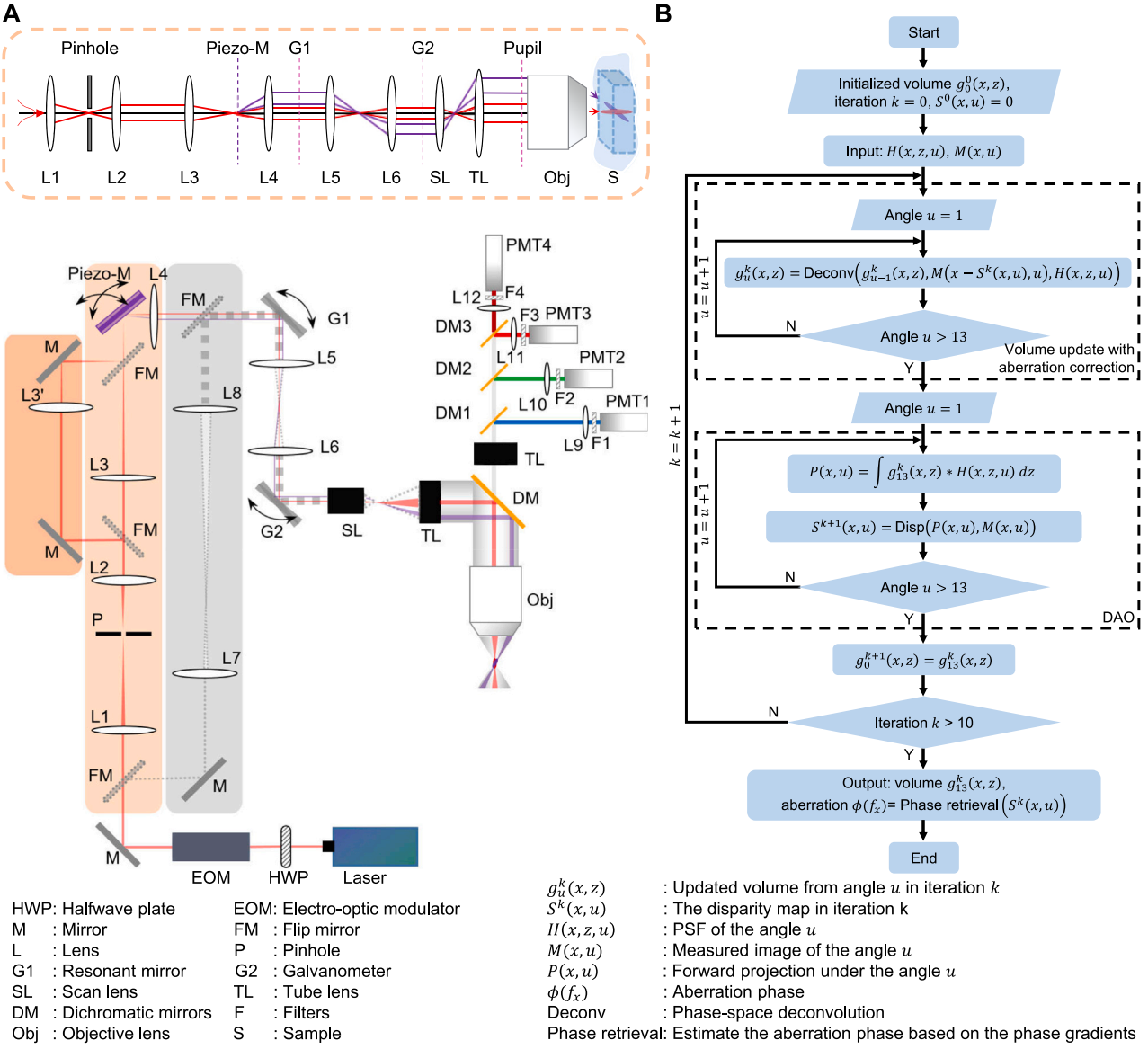

HWP: Halfwave plate
M : Mirror
L : Lens
G1 : Resonant mirror
SL : Scan lens
DM : Dichromatic mirrors
Obj : Objective lens
EOM: Electro-optic modulator
FM : Flip mirror
P : Pinhole
G2 : Galvanometer
TL : Tube lens
F : Filters
S : Sample

$g_u^k(x,z)$: Updated volume from angle u in iteration k
$S^k(x,u)$: The disparity map in iteration k
$H(x,z,u)$: PSF of the angle u
$M(x,u)$: Measured image of the angle u
$P(x,u)$: Forward projection under the angle u
$\phi(f_x)$: Aberration phase
Deconv : Phase-space deconvolution
Phase retrieval: Estimate the aberration phase based on the phase gradients

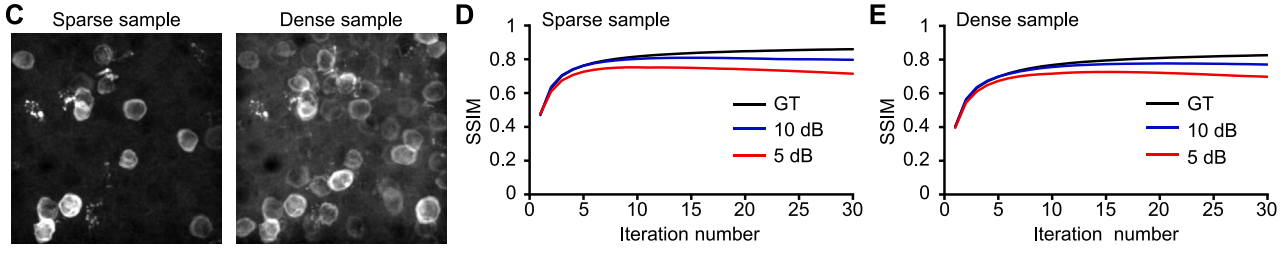

Figure S1. Illustration of experimental system and 3D reconstruction algorithm with DAO, related to Figure 1 and STAR Methods

(A) Schematic of the complete optical path of the experimental system with three configurations to be shifted for comparisons including traditional TPM, 2pSAM (mid), and 2pSAM (min). An intuitive diagram of 2pSAM is shown on the top. Electrical flip mirrors (FMs) were used to switch between different configurations

(legend continued on next page)

during experiments. 2pSAM can work as a compact add-on to existing TPM by adding a PSF modulation part at the beginning of the excitation path to generate needle-like correlated beams along different angles. A piezo-based mirror (Piezo-M) is used to change the angles of needle-like beams. Three configurations share the same lateral scanning path with a resonant mirror (G1) and galvo mirror (G2), and the detection path with four channels. We use the dichroic mirrors (DMs) and filters (F) to separate different wavelengths.

(B) Flowchart of the 3D reconstruction algorithm with DAO. The abbreviations used in the pseudo program are described in the bottom.

(C) Examples of the ground truth used during numerical simulations for both sparse and dense structures.

(D) The convergence curve of the algorithm on sparse samples in different SNR conditions, using structural similarity (SSIM) as the evaluation metric.

(E) The convergence curve of the algorithm on dense samples in different SNR conditions, using SSIM as the evaluation metric.

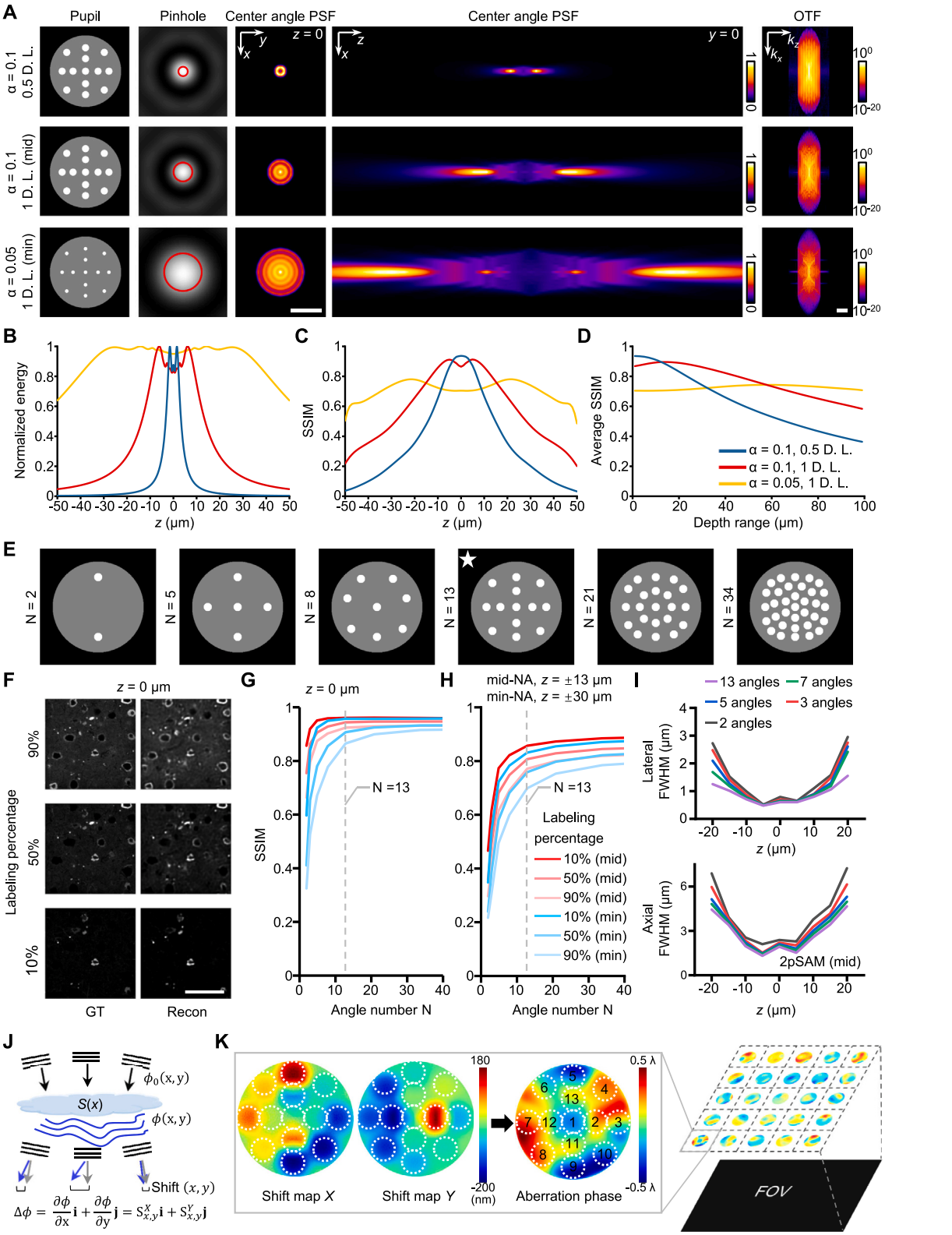

(legend on next page)

Figure S2. Influence of the pinhole size, sub-aperture NA, and angle number on 2pSAM performance illustrated by numerical simulation, related to Figure 1 and STAR Methods

(A) PSFs and OTFs of the center angle of 2pSAM with different values of ratio α and different pinhole sizes applied as those described in STAR Methods. We set the pinhole size as 0.5 and 1 D.L., marked by the red ring in the focal plane of the sub-aperture beam without pinhole. D.L. represents the Abbe diffraction limit of the sub-aperture NA. By adjusting the ratio α, we can balance the effective DOF and the spatial resolution when the number of angles is fixed. The OTFs on the right are obtained from the 3D Fourier transform of PSF and displayed on logarithmic scale.

(B) Normalized energy distributions along the axial domain of the PSFs with different sub-aperture NA (indicated by α) and different pinhole sizes.

(C) The SSIM between ground truth and reconstructed results with different sub-aperture NA (indicated by α) and different pinhole sizes at different axial planes. Small pinhole size will reduce the DOF, while large pinhole size will reduce the spatial resolution due to the relaxation of the ptychographic constraint. Large sub-aperture NA will reduce the DOF with better spatial resolution. We used the dense neural data generated in Figure S1C for numerical simulations.

(D) The average SSIM of different depth ranges for 2pSAM with different pinhole sizes and different sub-aperture NA. In our system, we chose the designed pinhole size as 1 D.L. and the ratio α as 0.1 for mid-NA 2pSAM to achieve near-diffraction-limited resolution with an effective volumetric range of 25 μm. For min-NA 2pSAM, we set the ratio α as 0.05 to achieve slightly reduced resolution with an effective volumetric range of about 100 μm.

(E) The distribution of the angles with different angle numbers used in 2pSAM during simulation.

(F) The reconstruction results of mid-NA 2pSAM compared with the ground truth (GT). We changed the labeling density of neurons (10%, 50%, and 90%) in simulation to analyze the reconstruction performance with different sample densities.

(G) Curves of the SSIM at the native objective plane versus the angle numbers used for different sample densities and sub-aperture NA configurations (mid-NA and min-NA).

(H) Curves of the SSIM at z = $\pm$13 μm in mid-NA 2pSAM and $\pm$30 μm in min-NA 2pSAM versus different angle numbers used for different sample densities.

(I) Curves of experimental average lateral and axial resolutions for mid-NA 2pSAM versus different axial planes with different numbers of angles used. The resolution is estimated by average FWHMs of the intensity profiles with a Gaussian fit for 200-nm-diameter beads distributed in 1% agarose (n = 400 beads, >10 beads per plane).

(J) Schematics illustrating that the local gradients of the aberration are proportional to the lateral shifts of corresponding sub-aperture components.

(K) The whole FOV can be divided into multiple small tiles with the overlap between each tile for multisite aberration correction. In each tile, the aberration wavefront can be integrated based on the gradient maps for each tile.

Scale bars: 5 μm and 1 μm^{-1} in (A) and 50 μm in (F).

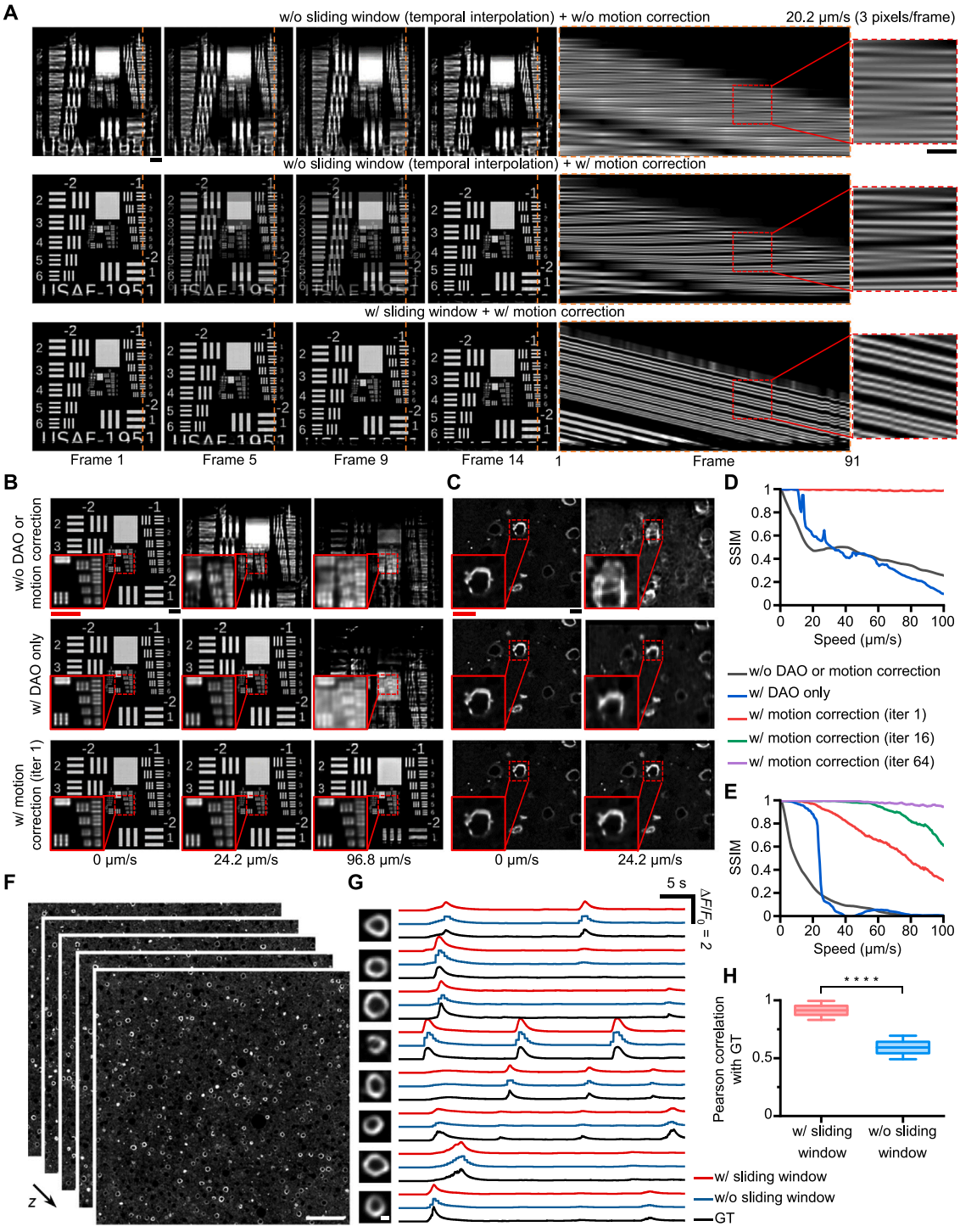

Figure S3. Quantitative evaluations of the motion-correction algorithm with a sliding window by numerical simulation, related to Figure 1 and STAR Methods

(A) Evaluation of the temporal resolution of 2pSAM for moving samples with and without the sliding window. The sample is simulated as moving at a speed of 3 pixels/frame. The reconstructed results of 2pSAM without a sliding window and motion correction, without a sliding window but with motion correction, and with a sliding window and motion correction, are shown from top to bottom. The kymograph with MIP along *xt* plane shows that the temporal resolution can be effectively improved by reconstruction with a sliding window and motion-correction algorithm. We use linear interpolation in the temporal domain for results without a sliding window.

(legend continued on next page)

(B) Evaluation of the reconstruction performance of samples with sharp edges (a resolution chart placed at the focal plane) with different motion speeds marked at the bottom during angle scanning. For the speed of 96.8 μm/s, the simulated sample shifts about 180 pixels during the scanning of 13 angles with each image of 512 × 512 pixels. We compare the results and zoom-in views in three different conditions, including without DAO or motion correction, with DAO only, and with motion correction of only 1 iteration.
(C) Evaluation of the reconstruction performance for the simulated 3D neurons with smooth structures during different levels of motion.
(D) Curves of the SSIM between the reconstructed result and the ground truth versus different moving speeds of the resolution chart, illustrating the effectiveness of the motion-correction algorithm and the intrinsic robustness of DAO algorithm.
(E) Curves of the SSIM between the reconstructed result and the ground truth versus different moving speeds of the 3D sample when multiple iterations were used in the motion-correction algorithm (1, 16, and 64 iterations). For 3D samples with smooth structures, more iterations used in the motion-correction algorithm can improve the robustness to motions. Only single iteration is also enough for large motions up to 54 pixels during angular scanning for the images with only 512 × 512 pixels (corresponding to the velocity of 30 μm/s for the 25×/1.05NA objective).
(F) Examples of the simulated time-lapse ground truth data of calcium dynamics generated by NAOMi used to analyze the temporal resolution of 2pSAM on functional dynamics.
(G) Calcium traces extracted from the ground truth and reconstructed results with and without a sliding window.
(H) Average Pearson correlation coefficients between the ground truth and reconstructed traces with and without a sliding window. We used mean ± standard deviation here (n = 100 traces for each method). Statistical significance was determined using one-way ANOVA with Dunnett's multiple comparisons test. ****$p < 0.0001$. Detailed parameters for simulation can be found in see STAR Methods.
Scale bars: 10 μm in (A); 10 μm in (B) and (C) (black for large FOV, red for zoom-in views); 20 μm in (F); and 5 μm in (G).

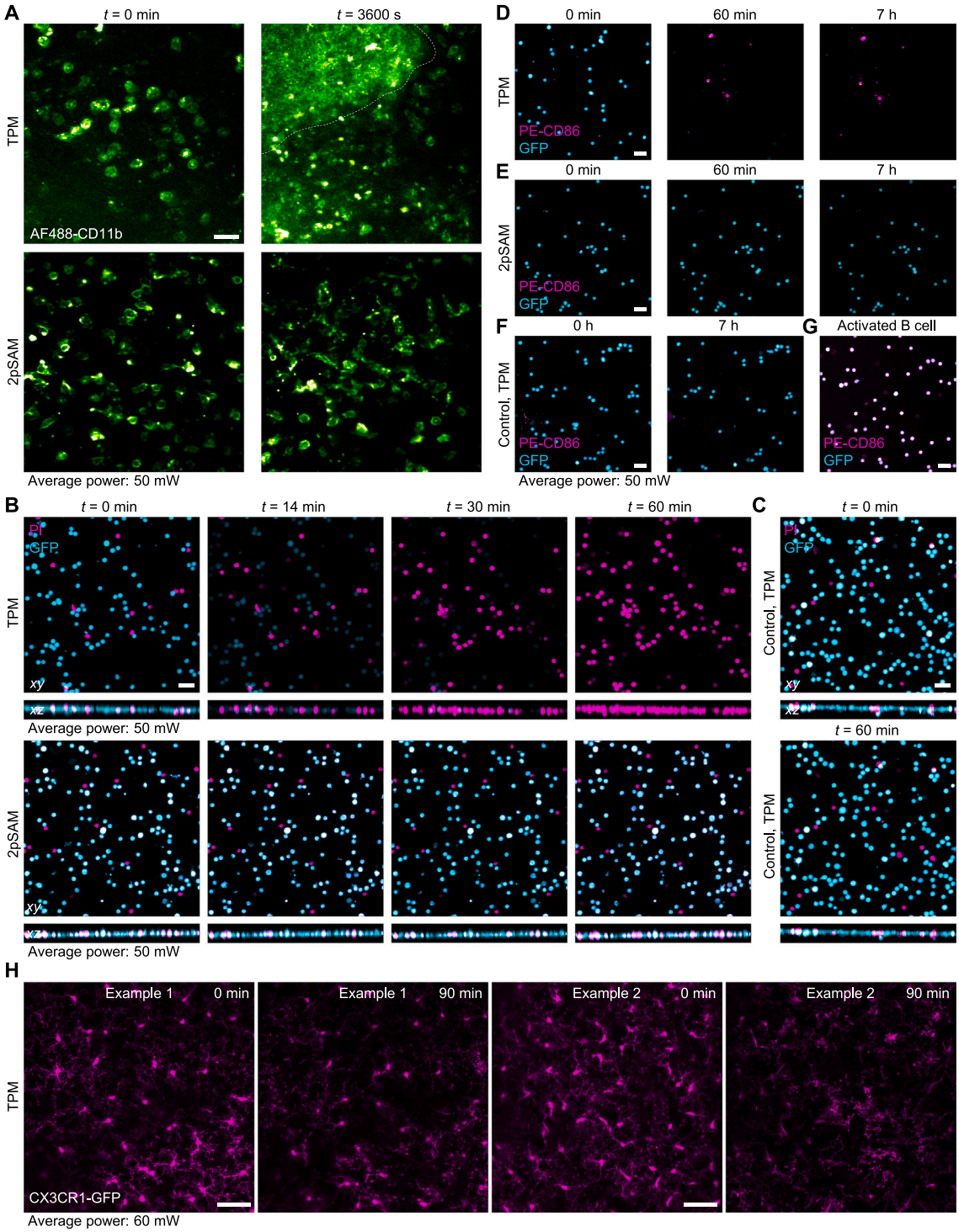

Figure S4. Evaluations of phototoxicity for TPM and 2pSAM, related to Figure 4

(A) MIPs of the immune cells (green, CD11b) in mice cortex immediately after craniotomy obtained by continuous imaging with TPM at different time points (39 axial slices at the interval of 1 μm) and 2pSAM (13 angles). The CD11b-labeled cells aggregated with the increase of autofluorescence signals in TPM after about half an hour, while the cells behaved naturally in mid-NA 2pSAM across an hour. We used the same laser power for comparisons marked at the bottom.

(B) Comparisons between TPM and 2pSAM during continuous *in vitro* imaging of isolated PI-labeled GFP-expressing B cells under the same laser power of 50 mW. MIPs at 4 time points are visualized.

(C) Control results obtained by TPM with only two volumes captured at 0 and 60 min. During the interval of an hour, the sample was not imaged.

(legend continued on next page)

(D) MIPs of GFP-expressing CD86-antibody-labeled B cells imaged by TPM at different time points. We imaged the sample with TPM for 1 h and then paused, and a volume was captured again after 6 h to guarantee the effectiveness of the antibody.
(E) MIPs of GFP-expressing CD86-antibody-labeled B cells imaged by 2pSAM at different time points under the same condition as (D). We imaged the sample with 2pSAM of the same CD86-injected GFP-labeled B cell cultures for 7 h continuously. The results demonstrated B cells were not activated during 2pSAM exposure.
(F) Control group experiment with two MIPs imaged by TPM at 0 and 7 h without continuous imaging.
(G) Positive control group experiment with the MIP of activated CD86-GFP-colabeled B cells imaged by TPM.
(H) Two examples of long-term imaging of microglia dynamic in the cortex of CX3CR1-GFP mice by TPM, illustrating large scale of cell death caused by accumulated photodamage.
Scale bars: 20 μm in (A)–(G) and 50 μm in (H).

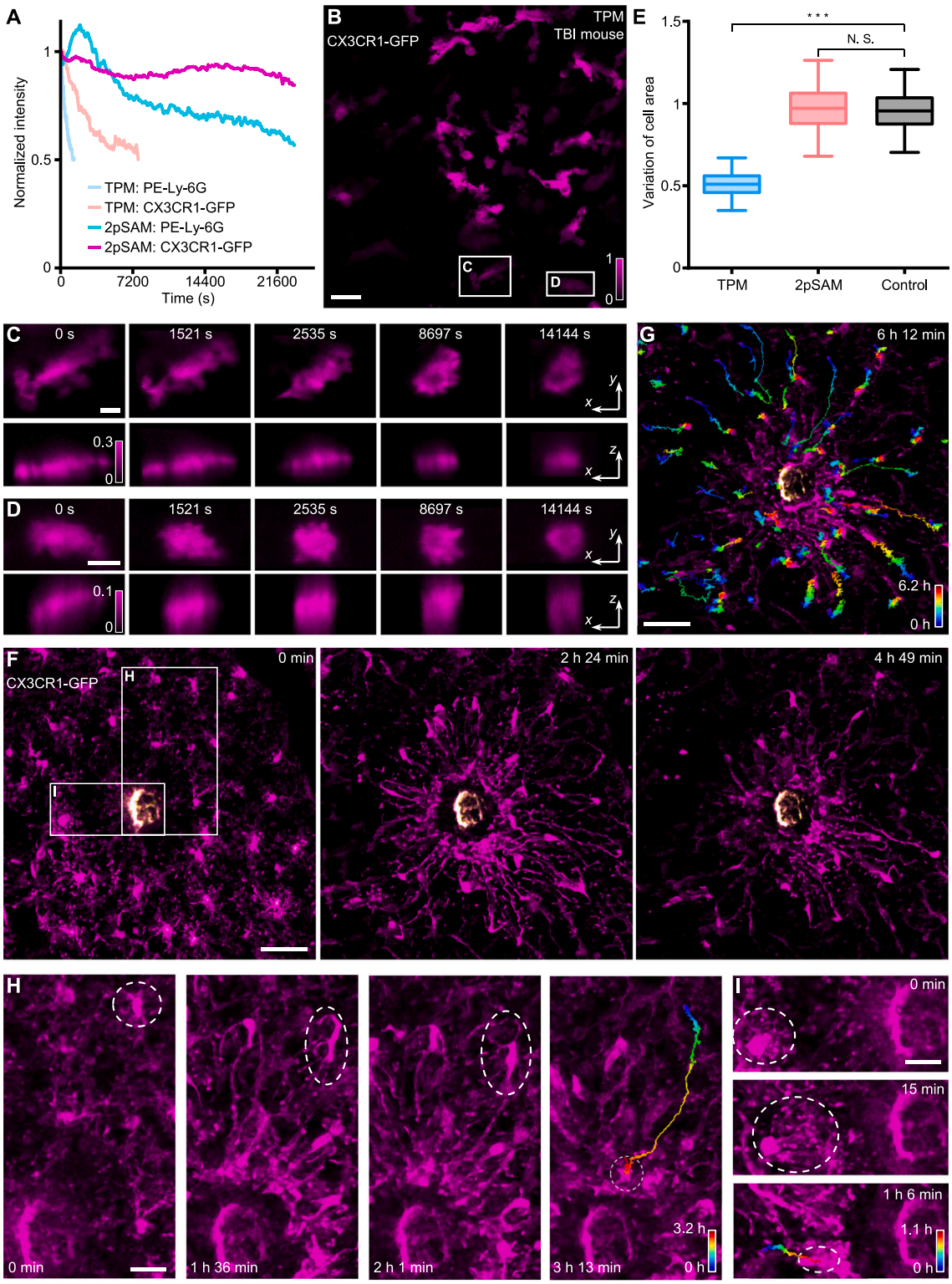

Figure S5. Comparisons between TPM and 2pSAM on the *in vivo* imaging of TBI mice, related to Figure 5

(A) Curves of normalized average fluorescence intensity versus time for two channels of TPM and 2pSAM during continuous imaging of neutrophils and CX3CR1-positive microglia/macrophages/monocytes in mouse cortex that follows TBI.

(B) MIP obtained by TPM of the TBI mouse after skull thinning at t = 0 s.

(legend continued on next page)

(C and D) Zoom-in *xy* and *xz* MIPs of two regions marked in (B) at different time points.
(E) Box plots of the variations of the cell area before and after 4 h for TPM, 2pSAM, and control group. We imaged the sample continuously within 4 h for TPM and 2pSAM, while we imaged only twice for the control group by TPM at 0 and 4 h. We used n = 3 different mice with 10 cells for each mouse. The variation of the cell area for each cell equals to the ratio between the cell area at 4 h and the cell area at 0 h.
(F) Laser-induced active dendritic behaviors and cell-body recruitments of microglia visualized by 2pSAM (mid). MIPs at different time points are shown. We induced laser injury by parking the 400-mW femtosecond laser for about 2 s in the center and imaged the microglia dynamics in CX3CR1-GFP mouse cortex with PE-Ly-6G labeling by mid-NA 2pSAM continuously for over 6 h at 3 volume/s.
(G) MIP with color-coded traces of soma overlaid at the last time point. Following laser-induced injury, the microglia first extended their tentacles to the damaged area, and finally migrated toward it. During this period, neutrophils in blood vessels were not observed to gather at the injury center.
(H) One microglia migrated from its original location to the injured area using about 3 h.
(I) Another example of microglia migration lasting for about 1 h. The dashed circles marked the soma position. Statistical significance was determined using one-way ANOVA with Dunnett's multiple comparisons test. N.S., not significant ($p > 0.05$); ***$p < 0.001$. We used mean ± standard deviation here. Scale bars: 20 μm in (B), (H), and (I); 10 μm in (C) and (D); and 50 μm in (F) and (G).

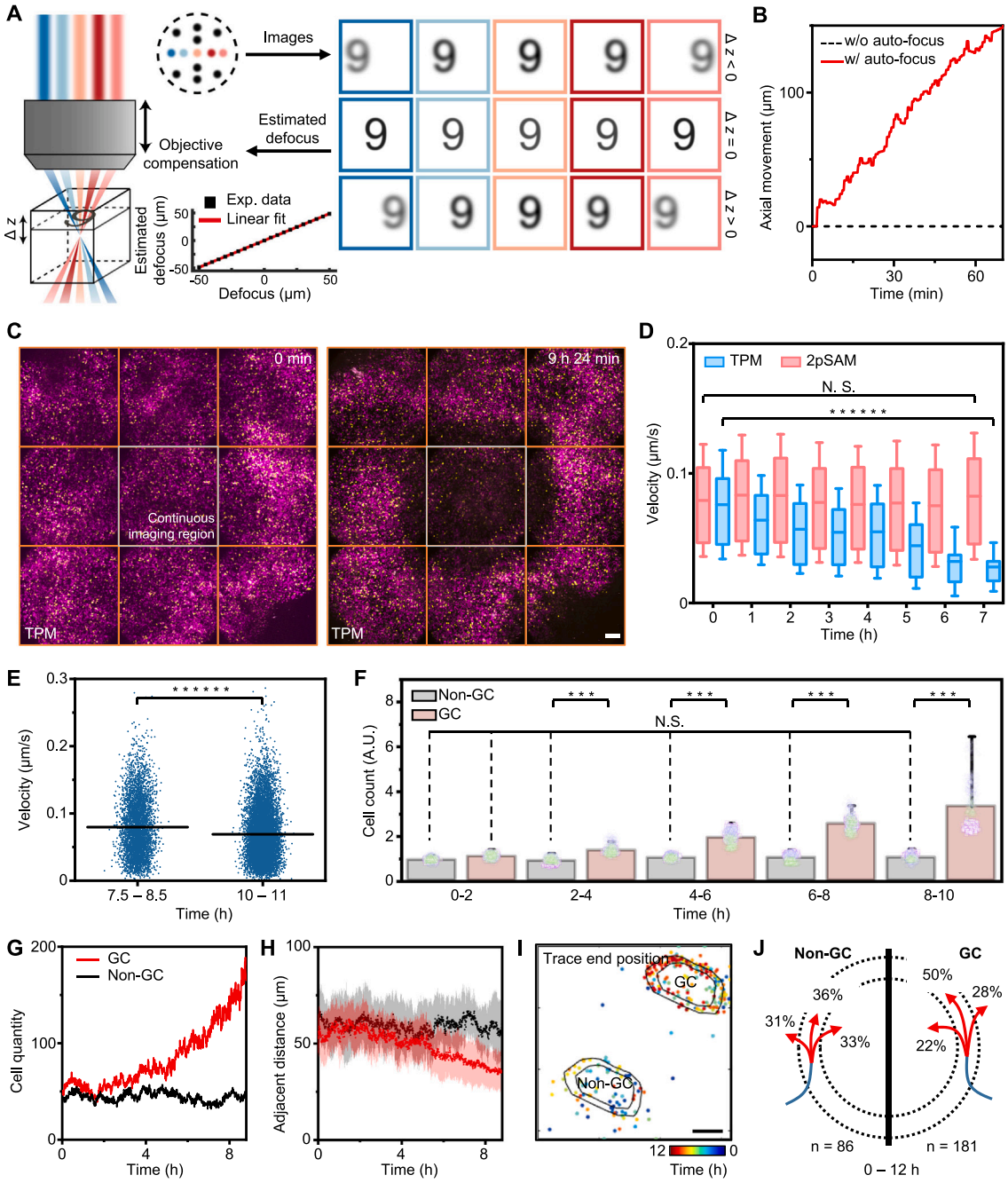

Figure S6. Comparisons between TPM and 2pSAM on the *in vivo* imaging of GC, related to Figure 6

(A) Illustrations of the autofocus method of 2pSAM. Since different sub-aperture components are captured by 2pSAM, the sample's defocus distance can be estimated directly by the disparities between different sub-aperture components, which can provide direct feedback for the objective stage to compensate sample movements.

(B) The accumulative axial movements of the objective during an *in vivo* imaging process of lymph node with and without autofocus.

(C) MIPs obtained by TPM at two time points. We imaged the process of GC formation in mouse lymph nodes *in vivo* by TPM with the same conditions as 2pSAM at 90 h after immunization. We captured and stitched the continuously imaged area and its surrounding area before the start of the recording and after 9 h 24 min of continuous recording for comparisons. Evident bleaching of the fluorescent signal could be observed in the area continuously exposed to TPM.

(D) Box plots of the velocities of B cells at different periods, illustrating the rapid decrease of the cell motility during continuous imaging of TPM. For each period, we randomly chose 1,000 cells for statistical analysis.

(E) Statistics of mean velocity of GC B cells before and after GC formation, corresponding to Figure 6E. Each dot represents one B cell and horizontal lines denote means.

(legend continued on next page)

(F) Average normalized B cell numbers in the GC and non-GC regions during the GC formation process. Data from 3 mice was collected. For every 2-h slot, we used the cell numbers at 200 random time points.
(G and H) Another experimental example recording the formation process of GC. The temporal changes of the total cell quantities in the GC and non-GC regions are shown in (G). The curves of the adjacent distances between cells versus time for the GC region and non-GC region are shown in (H).
(I) Overlay of the end positions for the traces of the B cells crossing the margin of the GC region and non-GC region for the data in Figure 6C. Different colors mean different time points.
(J) Frequencies of incoming B cell traces that ended in the outer GC/non-GC region or the GC/non-GC region or the 20 μm-buffer zone in between in Figure 6I. N.S., not significant ($p > 0.05$); ***$p < 0.001$; ******$p < 0.000001$. Statistical significance was determined using one-way ANOVA with Dunnett's multiple comparisons test. We used mean ± standard deviation here.
Scale bars: 100 μm in (C).

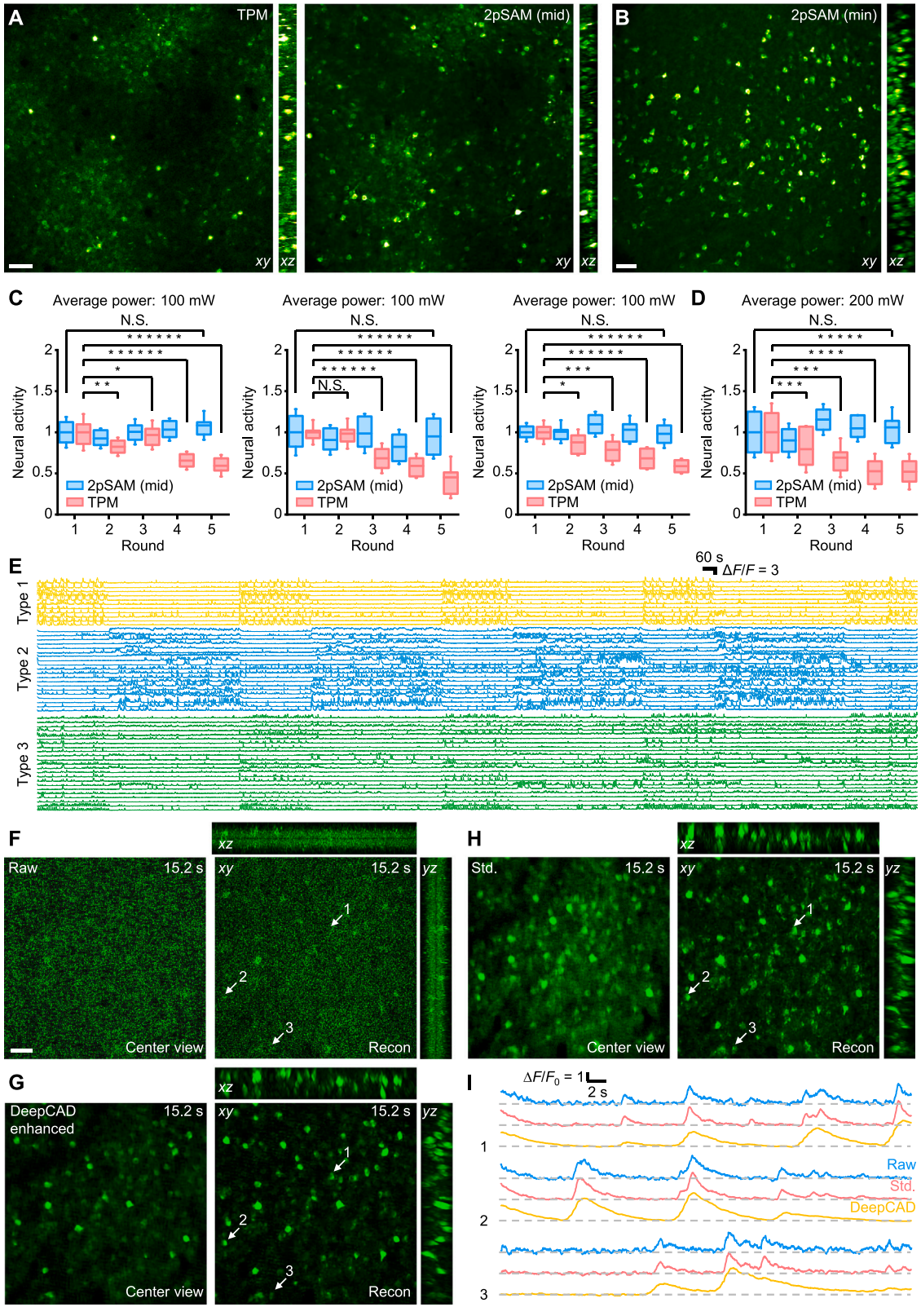

(legend on next page)

Figure S7. Comparisons between 2pSAM and TPM on large-scale neural imaging in mice, related to Figure 7

(A) Orthogonal MIPs of the standard deviation obtained by mid-NA 2pSAM (left) and TPM (right), respectively. We imaged the same region of the same mouse in the layer 2/3 cortical layer for comparisons.

(B) Orthogonal MIPs of the standard deviations of the volumes obtained by min-NA 2pSAM, illustrating larger volumetric coverage than mid-NA 2pSAM.

(C) Normalized average strength of neural activities during visual stimulus at 5 rounds for both TPM (red) and mid-NA 2pSAM (blue) with the same average laser power of 100 mW. We repeated the experiments 3 times with 6 mice. We used n = 20 neurons per mouse, selected based on the correlation to visual stimulus as described in STAR Methods.

(D) Normalized average strength of neural activities during visual stimulus at 5 rounds for both TPM (red) and mid-NA 2pSAM (blue) with the average laser power of 200 mW. We used n = 20 neurons per mouse, selected based on the correlation to visual stimulus as described in STAR Methods.

(E) All traces of the three types (type 1, type 2, and type 3) of neurons of interest are displayed, corresponding to the data in Figures 7H–7J. Type 1 is the neuron excited by grating stimulation. The other two types are the neurons that will be silent when grating stimulation occurs.

(F) The raw measurement of mid-NA 2pSAM for the center angle (left) and the reconstructed orthogonal MIPs using all-ones matrix as the initial value at 15.2 s (right). We conducted calcium imaging in the cortical layer 2/S3 of head-fixed Rasgrf2-2A-dCre;Ai148d mice with low power of 5 mW and resonant scanning.

(G) The center-angle measurement after applying the DeepCAD denoising algorithm at 15.2 s (left), and corresponding reconstructed orthogonal MIPs, illustrating that 2pSAM is compatible with existing two-photon imaging processing methods.

(H) The standard deviation of the raw center-angle data across 1,000 frames (left) and the reconstructed orthogonal MIPs at 15.2 s (right) using the standard deviation as the initial value. Considerably better contrast can be achieved by using the spatiotemporal sparse prior in neural imaging with 2pSAM.

(I) Comparisons of the reconstructed temporal traces of three neurons marked in (F)–(H). DeepCAD may reduce the temporal resolution with better SNR, while the sparse spatiotemporal prior can also enhance the SNR with preserved temporal resolution. We used the same data for these three methods for fair comparisons.

N.S., not significant ($p > 0.05$); *$p < 0.05$, **$p < 0.01$, ***$p < 0.001$, ****$p < 0.0001$, *****$p < 0.00001$, ******$p < 0.000001$, statistical significance was determined using one-way ANOVA with Dunnett's multiple comparisons test. We used mean ± standard deviation here.

Scale bars: 50 μm in (A) and (B) and 40 μm in (F), (G), and (H).